Am J Transl Res 2025;17(12):9422-9440
www.ajtr.org /ISSN:1943-8141/AJTR0169380

Original Article

Bu-Yi-Xin-Shen formula targets monocytes through PI3K-Akt/NF-κB signaling in post-percutaneous coronary intervention angina

Chunxiao Su[1*], Jinghui Bai[2*], Xiaomin Jiao[3]

*[1]Liaoning University of Traditional Chinese Medicine, Shenyang 100029, Liaoning, China; [2]Department of General Internal Medicine, Liaoning Cancer Hospital, Affiliated Cancer Hospital of Dalian University of Technology, Shenyang 110042, Liaoning, China; [3]The Second Affiliated Hospital of Liaoning University of Traditional Chinese Medicine, Shenyang 110034, Liaoning, China. *Equal contributors.*

Received October 17, 2025; Accepted December 1, 2025; Epub December 15, 2025; Published December 30, 2025

Abstract: Background: Bu-Yi-Xin-Shen formula (BYXSF) is used for the treatment of post-percutaneous coronary intervention (PCI) angina. This study combined bioinformatics and experimental verification to investigate its mechanism of action. Methods: We retrieved relevant target data from public databases to determine candidate therapeutic targets of BYXSF in post-PCI angina. Key targets were then determined using protein-protein interaction (PPI) network and functional enrichment assays. Molecular docking was used to identify core active ingredients, while toxicity evaluation helped assess their safety profiles. After that, single-cell RNA sequencing (scRNA-seq) uncovered critical cell types and the expression patterns of target genes. Finally, *in vivo* animal experiments provided evidence for the activation of pathways related to these key targets, further validating the proposed mechanism. Results: Functional enrichment analysis indicated that phosphatidylinositol 3-kinase-AKT (PI3K-Akt) and Nuclear factor kappa-light-chain-enhancer of activated B cells (NF-κB) signaling pathways were significantly enriched. Combined with the high interaction degree of genes in the PPI network, PIK3R1, PIK3CA, PIK3CB, EGFR, AKT1, and SRC were determined as key targets. Then, five active ingredients (benzoylnapelline, quercetin, liquiritigenin, sexangularetin, and deltoin) with the lowest binding energies (< -8 kcal/mol) were identified by molecular docking. These active ingredients were found to influence toxicity through processes including vascular inflammation and lipid metabolism/atherosclerosis. The scRNA-seq revealed monocytes as the core cell type mediating BYXSF's therapeutic effects, with distinct expression levels of key targets between high- and low-score groups. Finally, *in vivo* experiments confirmed that BYXSF alleviated post-PCI angina by regulating the PI3K-Akt and NF-κB signaling pathways. Conclusion: PIK3R1, PIK3CA, PIK3CB, EGFR, AKT1, and SRC were key genes in the PI3K-Akt and NF-κB pathways, and monocytes were major targets of BYXSF in post-PCI angina. Animal experiments validated this mechanism, laying a foundation for the further development of BYXSF as a therapeutic agent.

Keywords: Bu-Yi-Xin-Shen formula, network pharmacology, network toxicology, post-PCI angina, scRNA-seq

Introduction

Percutaneous coronary intervention (PCI) has become a basic revascularization technique for individuals with localized severe coronary artery disease. Although PCI significantly reduces the mortality associated with coronary artery disease, it can cause different degrees of vascular endothelial injury and inflammatory responses. Even after standard drug intervention, patients with recurrent angina continue to experience considerable stable angina symptoms [1]. The engagement of many pathogenic processes results in unique clinical manifestations and temporal symptom variability [2]. With their anti-inflammatory and antioxidant properties, statins can alleviate microvascular and vasospastic angina by reducing the frequency of angina pectoris and the incidence of cardiovascular events [3]. However, a recent meta-analysis did not find that any anti-angina pectoris drug had a significant advantage in improving myocardial ischemia and relieving angina symptoms [4]. Canadian Cardiovascular Society

https://doi.org/10.62347/CMPK4691

(CCS) guidelines [5] also clearly point out that there is currently no conclusive evidence to support the clinical superiority of specific types of anti-angina drugs.

Recent studies [6, 7] confirmed the efficacy of traditional Chinese medicine (TCM) in alleviating the recurrence of post-PCI angina. Bu-Yi-Xin-Shen Formula (BYXSF) contains eight herbal medicines: *Radix Salviae liguliobae*, *Radix Aconiti Lateralis*, *Radix Glycyrrhizae*, *Rhizoma Zingiberis*, *Ramulus Cinnamomi*, *Radix Astragali*, *Radix Ginseng*, and *Radix Notoginseng*. This prescription integrates the core ingredients of traditional prescriptions, creating a sophisticated mixture. Cinnamaldehyde contained in the *Ramulus Cinnamomi* has the properties of replenishes qi, enhancing cardiac function, inhibiting platelet aggregation, and anti-inflammatory [8]. Contemporary studies demonstrate that the principal bioactive components of *Rhizoma Zingiberis*, such as 6-gingerol, α-zingiberene, geraniol, and β-bisabolene, exhibit anti-inflammatory, lipid-lowering, anti-hypoxic [9], and cardioprotective properties [10]. *Radix Astragali* has several bioactive constituents, including glycosides, polysaccharides, and flavonoids [11]. Astragaloside IV (AS-IV), a key bioactive constituent of *Radix Astragali*, has been demonstrated to decrease the elevation of blood inflammatory factor levels [12]. *Radix Aconiti Lateralis*, a herb from the Aconitaceae family, is noted for its capacity to modulate heart rate, diminish myocardial oxygen consumption, and improve myocardial function [13]. *Radix Ginseng* contains ginsenosides (e.g., compound K and Rb1) that alleviate tumor necrosis factor-alpha (TNF-α)-induced oxidative stress, as well as oxidized low-density lipoprotein (ox-LDL)-triggered inflammation and apoptosis, ultimately mitigating angina symptoms [14, 15]. *Radix Salviae liguliobae*, rich in tanshinone IIA, exerts effects of inhibiting inflammatory factors, scavenging free radicals, protecting vascular endothelial cells, and suppressing cardiomyocyte apoptosis [16, 17]. *Radix Notoginseng* contains total saponins with anti-apoptotic, antioxidant, and anti-inflammatory effects. These compounds promote vascular endothelial cell proliferation, inhibit atherosclerosis development, prevent iron accumulation in organs like the liver and heart, protect myocardial cells, and reduce myocardial ischemia-reperfusion injury [18, 19]. Glycyrrhetinic acid, a key component of *Radix Glycyrrhizae*, reduces cardiomyocyte apoptosis, inhibits cardiac hypertrophy, and exhibits anti-ischemic activity [20]. Collectively, these eight herbs act through anti-inflammatory, anti-anginal, endothelial protective, and antiplatelet pathways, underpinning the therapeutic efficacy of BYXSF in post-PCI angina [21, 22]. The systematic activity and specific mechanism targets of BYXSF have rarely been studied and are worthy of further exploration.

Due to the complexity and multi-target nature of TCM compounds, network pharmacology based on systems biology has become a key tool to elucidate TCM mechanisms [23]. By analyzing the drug-disease interaction network, this method can reveal the synergistic effects of compound preparations. This study used network pharmacology to develop a herb-active ingredient-key target network, identified BYXSF's principal cell types in post-PCI angina at the single-cell level, and examined the expression of these targets. We employed a rat model of post-PCI angina to validate the therapeutic efficacy of BYXSF and quantify protein expression in essential signaling pathways, plus molecular docking to identify key active components and evaluate their potential toxicity. These results lay a foundation for understanding the molecular mechanism of the therapeutic benefits of BYXSF on angina after PCI and developing accurate treatment.

Materials and methods

Data collection

The single-cell RNA sequencing (scRNA-seq) dataset GSE184073 (GPL24676 platform) contained one stable angina pectoris (SAP) and one acute coronary syndrome (ACS) samples [24], was obtained from the Gene Expression Omnibus (GEO) database (http://www.ncbi.nlm.nih.gov/geo/).

Acquisition of drug target genes

Active ingredients of BYXSF were obtained by querying the Traditional Chinese Medicine Systems Pharmacology (TCMSP) database (https://old.tcmsp-e.com/tcmsp.php) with the following keywords: "*Radix Salviae liguliobae* (Chinese name: danshen)", "*Radix Aconiti Lateralis* (Chinese name: fuzi)", "*Radix Glycyrrhizae* (Chinese name: gancao)", "*Rhizoma Zingiberis* (Chinese name: ganjiang)", "*Ramulus Cinnamomi* (Chinese name: guizhi)", "*Radix* Astragali (Chinese name: huangqi)", "*Radix Ginseng*

(Chinese name: renshen)", and "*Radix Notoginseng* (Chinese name: sanqi)". The screening criteria were set as oral bioavailability (OB) ≥ 30% and drug-likeness (DL) ≥ 0.18. The PubChem database (https://pubchem.ncbi.nlm.nih.gov) was used to obtain the SMILES codes for these active ingredients. The associated target genes were then predicted using the SwissTargetPrediction database (http://swisstargetprediction.ch/). All drug target genes were compiled, and duplicates were removed to ensure data uniqueness. Target names were standardized by converting them into official gene symbols using the Universal Protein (UniProt) database (https://www.uniprot.org).

Identification of post-PCI angina target genes

Post-PCI angina target genes were identified through multi-database interrogation. GeneCards (https://www.genecards.org/), the Common Technical Document (CTD) (http://ctdbase.org/), and Online Mendelian Inheritance in Man (OMIM) (https://www.omim.org/) were queried with keywords such as "Post-PCI angina", "Angina after PCI", "Endothelial dysfunction", "Myocardial ischemia-reperfusion injury", and "Stable angina pectoris". Genes without UniProt IDs were excluded. Resulting targets from all databases were merged, and duplicates were removed to create a consolidated post-PCI angina target gene library for subsequent analysis.

Protein-protein interaction (PPI) network and functional annotation

The intersection of drug target genes and post-PCI angina target genes was determined. Kyoto Encyclopedia of Genes and Genomes (KEGG) and Gene Ontology (GO) enrichment analyses were performed on these intersecting genes using the DAVID database (https://david.ncifcrf.gov/) ($P < 0.01$). Three categories from the GO analysis - Molecular Function (MF), Cellular Component (CC), and Biological Process (BP) - were used to systematically characterize the roles of these target proteins in gene functional annotation. PPIs among intersection genes were predicted using STRING (v11.5) under high-stringency settings (confidence score ≥ 0.7; Homo sapiens). Cytoscape (v3.7.2) was utilized to visualize the network, and topological features (Degree, Betweenness, Closeness > median) were examined [25]. Genes located near the center of the PPI network, characterized by high connection scores, were identified as hub genes. Based on the enrichment results, hub genes within biological pathways significantly associated with post-PCI angina were prioritized for further mechanistic validation. KEGG enrichment analysis of these key targets was also performed ($P < 0.05$). To systematically investigate RNA crosstalk in the key target regulatory network, a long non-coding RNA (lncRNA)-microRNA (miRNA)-mRNA network was constructed. First, miRNA-mRNA interactions were predicted via miRTarBase (https://mirtarbase.cuhk.edu.cn/), then miRNA-lncRNA associations were identified using starBase (https://rnasysu.com/encori/). Finally, these relationships were integrated to map the RNA crosstalk mechanisms.

Molecular docking

To illustrate the complex relationships between the herbs, active ingredients, and key targets, a network was constructed and visualized using Cytoscape software. Molecular docking was employed to assess the binding affinity between the key targets and active ingredients using AutoDockTools (v1.5.7) [26]. The canonical 3D protein structures of the key targets were retrieved from the UniProt database in PDB file format. Structural optimization was carried out in AutoDockTools (v1.5.7), which included the merging of non-polar hydrogen atoms and assigning Kollman united-atom charges. Simultaneously, the 3D conformers of the active ingredients were obtained in SDF format from the PubChem database. Binding free energy (ΔG) values were calculated, with a threshold of ≤ -5.0 kcal/mol indicating favorable binding interactions.

Molecular dynamics (MD) simulation

Key active ingredients were identified based on their highest binding affinities with each key target. These docking results guided MD simulations using the Groningen Machine for Chemical Simulations (GROMACS) 2022 [27]. The ligand was modeled using the General AMBER Force Field (GAFF), while the protein was modeled with the AMBER14SB force field and the Transferable Intermolecular Potential 3-point (TIP3P) water model. The protein-ligand system was built by combining coordinate files and topologies. The NPT ensemble with periodic boundary conditions was employed for the simulations. To limit hydrogen bonding, the linear constraint solver (LINCS) algorithm was applied with a time step of 2 fs. The Particle Mesh Ewald (PME) method was used to handle long-range electrostatics with a cutoff of 1.2 nm, while non-bonded interactions were truncated at 1.0 nm. Neighbor lists were updated every ten steps. Temperature (298 K) and pressure (1 bar) were controlled using the V-rescale thermostat and the Berendsen barostat, respectively. After the initial system equilibration, which included 100 ps in the canonical ensemble (NVT) and 100 ps in the isothermal-isobaric ensemble (NPT) phases, a 100 ns NPT production run was performed, saving coordinate snapshots every 10 ps. Stable trajectory segments were selected based on root mean square fluctuation (RMSF), root mean square deviation (RMSD), buried solvent accessible surface area (buried SASA), radius of gyration (Rg), and interaction energy. Binding energy and its components were subsequently analyzed using the MM-PBSA method.

Toxicity evaluation and pharmacokinetic properties of the key active ingredients

The pharmacokinetic properties of the key active ingredients were evaluated using the SwissADME platform (http://www.swissadme.ch/). Subsequently, the key active ingredients were input into the ProTox 3.0 server (https://tox.charite.de) for a safety evaluation, which predicted organ-specific toxic effects, including hepatotoxicity, cardiotoxicity, nephrotoxicity, neurotoxicity, and respiratory toxicity. These toxicity predictions were cross-referenced with the OMIM and GeneCards databases (Relevance.score > 6) to identify genes associated with toxicity. By combining gene lists and removing duplicate genes, a set of non-redundant visceral toxicity targets was developed. Simultaneously, the toxicological targets associated with principal active ingredients were forecasted by amalgamating the SwissTargetPrediction platform (http://www.swisstargetprediction.ch/), the Comparative Toxicogenomics Database (CTD), and the Chemical Substance Interaction Search Tool (STITCH) database (http://stitch.embl.de), followed by integration and redundancy removal. The intersection of these two target sets revealed common toxicity targets, leading to a streamlined list.

Cell annotation

The GSE184073 dataset was filtering, quality control, clustering, and annotation by the Seurat package (v5.1.0) [28]. Firstly, we retained data in this dataset where nFeature_RNA < 4,000, nCount_RNA < 20,000, and percent.mt < 15% for analysis. After logarithmic normalization, the vst method was used to select the top 2,000 highly variable genes (HVGs), which were then subjected to principal component analysis (PCA). The optimal principal components (PCs) for downstream clustering were selected based on permutation testing and scree plot interpretation. Cell clustering was performed using the FindNeighbors and FindClusters functions at a resolution of 0.1, and the results were visualized using Uniform Manifold Approximation and Projection (UMAP) for dimensionality reduction. Cell types were annotated by cross-referencing cluster-specific marker genes with the existing literature [24]. Additionally, DoubletFinder (v2.0.4) was employed to detect and remove potential doublets [29].

Identification of critical cell types

To assess the intersection gene scores across different cell types in the GSE184073 dataset, five gene signature scoring approaches - AUCell (calculating 'Area Under the Curve' for gene set enrichment in individual cells), UCell (a Mann-Whitney U-statistic-based cell scoring method), singscore, single-sample Gene Set Enrichment Analysis (ssGSEA), and Seurat's AddModuleScore - were used. Cell types yielding the highest scores were identified as critical. These critical cell types were categorized into high/low-score groups based on the average score of each cell type across the entire cohort. The expression levels of key targets were then compared between these two groups to identify significant differences ($P < 0.05$). Finally, pseudotime trajectory analysis of the critical cell types was conducted using the Monocle (v2.26.0) package [30].

Animal grouping

A total of 60 specific pathogen-free (SPF) male Sprague Dawley (SD) rats, aged 6-8 weeks and weighing 270±20 g, were purchased from Liaoning Changsheng Biotechnology Co., Ltd. (SCXK (Liao) 2020-0001). All animal experiments were approved by the Animal Ethics Committee of the Liaoning Provincial Institute of Traditional Chinese Medicine (Approval No. LZYY250608) and conducted in accordance with the National Institutes of Health (NIH) Guide for the Care and Use of Laboratory Animals. The rats were housed in an SPF (specific pathogen-free) animal facility at Changchun University of Chinese Medicine, where the temperature was maintained between 20-26°C, with 50±5% relative humidity, 15-20 air changes per hour, and noise levels under 60 dB. A standard 12-hour light/dark cycle was implemented, and the rats were provided standard rodent feed and unlimited access to water. After a one-week acclimatization period, the body weights of all rats were measured, and they were randomly grouped for drug intervention. The 60 rats were divided into six groups, with ten rats per group: sham-operated group (S group), ischemia/reperfusion model group (I/R group), low-, medium-, and high-dose BYXSF groups (BYXSF-L, BYXSF-M, BYXSF-H: 7.03 g, 14.06 g, 28.12 g crude drug/kg/day, respectively), and the atorvastatin group (4 ml/kg/day). All drug treatments were prepared as 6 ml daily per rat and administered by oral gavage in two 3 ml doses (morning and evening). The S and I/R groups were administered an identical volume of saline through oral gavage twice daily. Drug intervention lasted for 28 consecutive days. Blood samples were then collected from the abdominal aorta. To extract serum, blood was allowed to clot for 30 minutes at 4°C and then centrifuged at 3000 g for 15 minutes. A portion of the cardiac tissue was immediately washed with cold phosphate-buffered saline (PBS) and fixed in 4% paraformaldehyde (PFA) for at least 24 hours. All serum and non-fixed tissue samples were stored at -80°C until further analysis.

Animal modeling

Both the I/R and drug intervention groups underwent ischemia surgery. After induction with 4% isoflurane anesthesia (RWD Life Science, R510-22-10), the rats were placed in an induction chamber connected to an anesthetic vaporizer. An isoflurane-oxygen mixture was delivered through a nose cone to maintain anesthesia. A thoracotomy was performed at the left third to fourth intercostal space to expose the heart. Using 6-0 silk sutures (Ethicon, 8610H) and a 2-mm polyethylene rod, the left anterior descending coronary artery (LAD) was ligated to induce myocardial ischemia. Successful occlusion was confirmed by the immediate pallor of the cardiac apex and a marked decrease in fractional shortening (FS) observed through echocardiography. Reperfusion was initiated by releasing the ligature and rod 30 minutes after occlusion and maintained for 120 minutes. Successful reperfusion was indicated by the return of red coloration to the apex and a sustained reduction in FS > 40%. In the S group, the surgical procedure was identical, except that the LAD was not ligated. Air in the thoracic cavity was evacuated using a syringe, and the intercostal space, muscle layers, and skin were closed.

Evaluation of cardiac function

Hair from the rats' chest and abdomen was first removed using depilatory cream. After anesthetizing the rats with 2% isoflurane, they were fixed in the supine position on the workbench. An ultrasonic coupling agent was evenly applied to the left anterior wall and extremities. The rats' electrocardiogram and respiratory status were monitored. The ultrasonic probe was manually adjusted and fixed in the correct position, and corresponding data were recorded. After the procedure, the rats were removed, the coupling agent was wiped off, and they were placed in a cage to recover. Data were analyzed using the software provided with the ultrasonic instrument, and the left ventricular ejection fraction (EF%) and left ventricular FS (FS%) were measured by echocardiography. At the experimental endpoint, rats were anesthetized with carbon dioxide (CO_2) at a flow rate of 5.8 L/min for 2 minutes. Once the rats exhibited a loss of corneal reflex and ceased voluntary limb movement, CO_2 delivery continued for an additional 12 minutes. After discontinuing the gas supply, a 2-minute observation period was implemented to confirm the absence of spontaneous respiration and corneal reflex.

Histologic staining

The fixed cardiac tissue specimens were successively dehydrated with gradient ethanol solution, and then embedded and sectioned (4-5 μm). Subsequently, the sections were deparaffinized in xylene, rehydrated step by step to distilled water through a gradient ethanol series, and then stained with hematoxylin and eosin (H&E). After staining was completed, the specimens were dehydrated by a gradient ethanol series, transparent with xylene twice (4 minutes each), and finally sealed with neutral resin for microscopic observation and imaging.

Following harvesting, cardiac samples were submerged in ice-cold PBS and swiftly moved to a -20°C freezer for 30 minutes to enable sectioning. The frozen tissues were cut transversely into six 2-mm thick slices, starting from the apex toward the base. These slices were incubated in a 37°C water bath containing a 2% solution of 2,3,5-triphenyltetrazolium chloride (TTC, Solarbio, T8170) for 30 minutes, protected from light. After staining, the slices were rinsed in PBS for 3 minutes, gently blotted dry, and immediately photographed for infarct size quantification.

TdT-mediated dUTP Nick-End Labeling (TUNEL) staining

Following dissection, the myocardium at the apex of the rat hearts in each group was randomly selected for conventional fixation, dehydration, paraffin embedding, sectioning, dewaxing in xylene, and ethanol gradient dehydration. A 100 μL solution of Proteinase K working solution (98 μL of PBS and 2 mL of 50 X Proteinase K) was used to digest tissues at 37°C for 30 minutes. The samples were then treated with 3% H_2O_2 at room temperature for 5 minutes, followed by incubation with 1% Triton X-100 citric acid solution on ice for 4 minutes to allow permeation, and rinsed with PBS. TUNEL reaction mixture (50 μL, Sigma, 11684795910) was added and incubated at 37°C for 60 minutes, followed by PBS rinsing. After incubation with peroxidase (POD, 50 μL) at 37°C for 30 minutes, 100 μL of 3,3-diaminobenzidine (DAB) chromogenic solution was added, and the samples were observed under a microscope. The samples were lightly stained with hematoxylin and then subjected to routine dehydration, clearing, and mounting. Results were analyzed using Motic Images Advanced 3.2 software, with quantification based on grayscale values.

Enzyme-linked immunosorbent assay (ELISA)

The concentrations of inflammatory mediators, including interleukin-1β (IL-1β, ABclonal, RK00009), TNF-α (ABclonal, RK00029), cardiac troponin I (cTnI, Shanghai Enzyme-linked Biotechnology Co., Ltd., ml003202), and creatine kinase-MB (CK-MB, Shanghai Enzyme-linked Biotechnology Co., Ltd., ml059533), were quantified in serum using ELISA, following the manufacturer's instructions for the reagent kits (Shanghai Enzyme Linked Biotechnology Co., Ltd.).

Reverse transcription quantitative real-time PCR (RT-qPCR)

Total RNA was extracted from cardiac tissues using Trizol reagent. RNA concentration and the OD260/OD280 ratio were measured using a spectrophotometer. The RNA was then reverse-transcribed into complementary DNA (cDNA) using a reverse transcription kit (ABclonal, RK20429), under the following conditions: 37°C for 2 minutes, 55°C for 15 minutes, 85°C for 5 minutes, followed by a 4°C hold. RT-qPCR was conducted using the Genious 2X SYBR Green Fast qPCR Mix (ABclonal, RK21204) with the following thermal cycling parameters: initial denaturation at 95°C for 3 minutes, followed by 40 cycles of denaturation at 95°C for 5 seconds and annealing/extension at 60°C for 30 seconds. Relative mRNA expression levels were calculated using the $2^{-\Delta\Delta CT}$ method. The primer sequences used for RT-qPCR are listed in **Table 1**.

Western blotting

Total protein was extracted from frozen cardiac tissue and quantified using the radio immunoprecipitation assay (RIPA, Solarbio, R0010) buffer (1:5) and a bicinchoninic acid (BCA) protein kit (Solarbio, R0020). Samples containing 40 μg of protein in 20 μL were separated by sodium dodecyl sulfate-polyacrylamide gel electrophoresis (SDS-PAGE), followed by electrophoretic transfer onto nitrocellulose membranes. The membranes were blocked for 1 hour at room temperature with 5% (w/v) non-fat dry milk. After blocking, membranes were incubated overnight at 4°C with primary antibodies: p-AKT (1:1000), AKT (1:30000), p-NF-κB P65 (1:20000), NF-κB P65 (1:500), p-PI3K (1:500), PI3K (1:30000), and GAPDH (1:100000) (Servicebio), all diluted in blocking buffer. Membranes were then rinsed with TBST and incubated with secondary antibody (Rabbit anti-rat IgG-HRP, 1:500) in blocking buffer for 1 hour at room temperature. After extensive washing with Tris Buffered Saline with Tween

Table 1. Primer sequences used for RT-qPCR

Name	Sense primer	Anti-sense primer	Length (bp)
AKT	GAGGAGCGGGAAGAGTG	GTGCCCTTGCCCAGTAG	200
PI3K	ATCACTGGCTCAAGGAA	ACCTATCCCAAGAACAAA	113
NF-κB	GAGGAAACGCCAGAAGC	GCAATCCCACCGTAAGC	177

20 (TBS-T), immunoreactive bands were detected using an enhanced chemiluminescence (ECL) substrate (Tanon 180-5001). ECL reagent was applied following the manufacturer's guidelines, and the bands were analyzed using ImageJ 1.8.0 software. Band intensity (optical density) was quantified using ImageJ, with GAPDH (Protein Biology) as the loading control for normalization.

Statistical analysis

Statistical analyses were performed using R software. Group differences were evaluated using the Wilcoxon test, with statistical significance set at $P < 0.05$. A normality test was performed on the measured data. For samples with a normal distribution, data were expressed as mean ± standard deviation (Mean ± SD). The t-test was employed for comparing the differences between two groups, while one-way analysis of variance (one-way ANOVA) was used to compare the means among multiple groups. For pairwise comparisons following one-way ANOVA, the Bonferroni test was applied when variances were homogeneous, and Dunnet's T3 test was adopted when variances were heterogeneous. All statistical tests were two-tailed, and a $P < 0.05$ was considered significant. All data analyses were conducted using SPSS 26 statistical software, and graphing and image processing were performed using GraphPad Prism 9.5.1.

Results

PIK3R1, PIK3CA, PIK3CB, EGFR, AKT1, and SRC were key targets

A total of 157 active ingredients were identified across the herbal constituents: Radix Salviae liguliobae (17), Radix Aconiti Lateralis (14), Radix Glycyrrhizae (88), Rhizoma Zingiberis (5), Ramulus Cinnamomi (6), Radix Astragali (19), Radix Ginseng (17), and Radix Notoginseng (7). These active ingredients corresponded to 941 drug target genes (Table S1). After deduplication, 7,851 post-PCI angina target genes were identified through integrated analysis of multiple databases (Table S1). Of these, 775 intersection genes were shared between the two sets of target genes (Figure S1A). These intersection genes were significantly enriched in 30 KEGG pathways and 20 GO terms, including the phosphatidylinositol 3-kinase-AKT (PI3K-Akt) and Nuclear factor kappa-light-chain-enhancer of activated B cells (NF-κB) signaling pathways signaling pathways, the AGE-RAGE signaling pathway in diabetic complications (inflammation), as well as pathways related to drug response (BP), membrane rafts (CC), and drug binding (MF), among others (Figure S1B, S1C). In the PPI network, targets with Degree > 25, Betweenness > 3942.3078, and Closeness > 0.039823409 were selected, resulting in a subnetwork comprising 72 genes and 721 interaction pairs (Figure S1D). Hub genes located at the network's topological centers included TP53, SRC, AKT1, STAT3, HSP90AA1, JUN, ESR1, MAPK1, PRKACA, MAPK3, PIK3R1, EP300, PIK3CA, EGFR, and PIK3CB. Given the pivotal roles of the PI3K-Akt and NF-κB signaling pathways in angina pathogenesis and the enrichment of intersection genes, the related hub genes PIK3R1, PIK3CA, PIK3CB, EGFR, AKT1, and SRC were selected as key targets for further investigation. KEGG pathway enrichment analysis independently confirmed significant enrichment of these hub genes in the PI3K-Akt signaling pathway (Figure S1E; Table S2). Further analysis identified 54 miRNAs targeting the key genes and 29 lncRNAs interacting with these miRNAs. The constructed lncRNA-miRNA-mRNA network illustrated complex regulatory relationships, such as the co-regulation of AKT1, EGFR, PIK3CA, and PIK3R1 by OIP5-AS1, NORAD, and MIR17HG through hsa-miR-155-5p (Figure S1F).

The active ingredients exhibited strong binding affinity with key targets

The herb-active ingredient-key target network comprised six herbs, six key targets, and 20 active ingredients (Figure S2A). The binding energies between these key targets and active ingredients were all below -5 kcal/mol, indicating strong binding affinities (**Table 2**).

Table 2. Binding energy of key targets and drug active ingredients

Herb	Molecule	PubChem CID	Symbol	Identifier	Energy
fuzi	benzoylnapelline	102549350	AKT1	4GV1	-8.3
renshen	Girinimbin	96943			-8.5
gancao	kaempferol	5280863			-7.7
huangqi	kaempferol	5280863			-7.7
renshen	kaempferol	5280863			-7.7
danshen	luteolin	5280445			-8.1
gancao	naringenin	439246			-8.1
gancao	Quercetin	5280343			-8.0
huangqi	Quercetin	5280343			-8.0
sanqi	Quercetin	5280343			-8.0
ganjiang	Sexangularetin	5281698			-7.5
fuzi	Deltoin	906525	EGFR	1IVO	-8.1
fuzi	Deoxyandrographolide	21679042			-7.9
renshen	Girinimbin	96943			-8.2
renshen	kaempferol	5280863			-8.1
fuzi	Karanjin	100633			-8.0
danshen	luteolin	5280445			-8.4
huangqi	Quercetin	5280343			-8.4
sanqi	Quercetin	5280343			-8.4
ganjiang	Sexangularetin	5281698			-8.3
fuzi	benzoylnapelline	102549350	PIK3CA	2RD0	-8.1
fuzi	Deltoin	906525			-8.9
fuzi	Deoxyandrographolide	21679042			-8.3
sanqi	DFV	114829			-9.2
huangqi	isoflavanone	160767			-8.6
fuzi	Karanjin	100633			-8.5
fuzi	Deltoin	906525	PIK3CB	AF_P42338_F1	-7.7
sanqi	DFV	114829			-8.5
huangqi	isoflavanone	160767			-7.5
fuzi	Karanjin	100633			-8.1
renshen	Frutinone A	441965	PIK3R1	8ILV	-8.2
renshen	kaempferol	5280863			-8.0
ganjiang	Sexangularetin	5281698			-8.3
fuzi	benzoylnapelline	102549350	SRC	2BDJ	-8.7
fuzi	Deltoin	906525			-9.6
sanqi	DFV	114829			-9.4
renshen	kaempferol	5280863			-9.6
fuzi	Karanjin	100633			-9.0
danshen	NSC 122421	94162			-9.4
ganjiang	Sexangularetin	5281698			-9.6

Specifically, AKT1 bound to benzoylnapelline, girinimbin, kaempferol, luteolin, naringenin, quercetin, and sexangularetin, while EGFR interacted with deltoin, deoxyandrographolide, girinimbin, kaempferol, karanjin, luteolin, quercetin, and sexangularetin. PI3K family members showed distinct compound affinities: PIK3CA bound to benzoylnapelline, deltoin, deoxyandrographolide, liquiritigenin (DFV), isoflavanone, and karanjin; PIK3CB engaged with deltoin, DFV, isoflavanone, and karanjin, and PIK3R1 specifically interacted with frutinone

A, kaempferol, and sexangularetin. SRC exhibited the broadest binding spectrum, interacting with benzoylnapelline, deltoin, DFV, kaempferol, karanjin, NSC 122421, and sexangularetin. Molecular docking identified six optimal ligand-target pairs with the lowest binding energies: AKT1-benzoylnapelline (-8.3 kcal/mol), EGFR-quercetin (-8.4 kcal/mol), PIK3CA-DFV (-9.2 kcal/mol), PIK3CB-DFV (-8.5 kcal/mol), PIK3R1-sexangularetin (-8.3 kcal/mol), and SRC-deltoin (-9.6 kcal/mol) (Figure S2B-G). Girinimbin had the highest binding energy with AKT1 (-8.5 kcal/mol) but was omitted from essential components due to the absence of hydrogen bond interactions. The chosen key active components, distinguished by advantageous binding affinities and particular molecular interactions, were prioritized for MD modeling. During the simulation process, the RMSD, Rg, and buried SASA values of the main active ingredient-key target complexes reached stabilization, and the RMSF amplitude and hydrogen bond analysis indicated that the structures were stable. ΔG calculations indicated significant thermodynamic stabilization across all complexes, with PIK3CA-DFV exhibiting the strongest interaction energy (ΔGbind = -161.78±2.07 kJ/mol), followed by PIK3R1-sexangularetin (-120.44± 3.70 kJ/mol), SRC-deltoin (-115.35±3.20 kJ/mol), PIK3CB-DFV (-102.21±5.05 kJ/mol), EGFR-quercetin (-92.39±13.21 kJ/mol), and AKT1-benzoylnapelline (-24.18±8.22 kJ/mol) (**Table 3**).

Pharmacologic properties of key active ingredients

ADMET analysis thoroughly delineated the principal active constituents, with molecular weights ranging from 266.25 to 328.36 Da, lipophilicity (LogP) values between 1.99 and 3.38, 4 to 6 hydrogen bond acceptors, 0 to 5 hydrogen bond donors, and topological descriptors such as polar surface area (66.32-131.36 $Å^2$) (Figure S3A-E). All key active ingredients also showed high gastrointestinal absorption. Benzoylnapelline, deltoin, and DFV demonstrated the capacity to penetrate the blood-brain barrier (BBB), whereas quercetin and sexangularetin had restricted access to the central nervous system (CNS). P-glycoprotein substrate status was confirmed for benzoylnapelline and DFV. Cytochrome P450 inhibition profiles were compound-specific: benzoylnapelline inhibited CYP2C19/2D6, deltoin inhibited CYP1A2/2C19/2C9/3A4, DFV inhibited CYP1-A2, and quercetin and sexangularetin inhibited CYP1A2/2D6/3A4. Skin permeation potential ranged from -7.05 to -5.68 cm/s across the series (**Table 4**).

Active ingredients affected toxicity through multiple approaches

Computational toxicity profiling revealed multi-organ liabilities. Benzoylnapelline exhibited neurotoxic, nephrotoxic, and respiratory risks, while sexangularetin showed cardiotoxic potential along with nephrotoxic and respiratory toxicity. DFV and quercetin shared nephro-respiratory dual toxicity, and deltoin displayed respiratory toxicity (Figure S4A-E). These toxicity predictions were further validated by searching public databases to identify associated toxicity targets. After deduplication, 2,334 visceral toxicity targets and 4,633 key active ingredient-related toxicity targets were identified, resulting in 948 common toxicity targets (Figure S4F). GO enrichment analysis revealed 5,409 enriched terms related to common toxicity targets, including 4,807 BPs, 248 CCs, and 354 MFs. Pathways associated with hypoxia, oxidative stress, and nutrient response were potentially linked to post-PCI angina. KEGG pathway analysis highlighted 230 enriched pathways, including lipid metabolism, atherosclerosis, TNF signaling, and calcium signaling, which could mediate disease progression (Figure S4G, S4H). These findings suggest a role for vascular inflammation, lipid metabolism/atherosclerosis, oxidative stress, calcium signaling-mediated vascular/myocardial dysfunction, and impaired myocardial energy metabolism in the pathogenesis of post-PCI angina.

Monocytes emerged as the critical cell type

After quality control, scRNA-seq analysis of 2,062 cells and 19,292 genes identified six clusters based on the top 30 PCs in PCA (**Figures 1A**, S5A-D). Four cell types were annotated, including mast cells, monocytes, dendritic cells, and macrophages, with mast cells and monocytes being the predominant populations (**Figures 1B**, **1C**, S5E). Following the removal of 155 doublets (7.5%), clear inter-population boundaries emerged (Figure S5F). Monocytes were identified as the critical cell type due to their elevated activity of intersection genes (mean composite score from 5 algorithms),

Table 3. Energy terms related to the binding energy of key active ingredients and key targets

Complex	ΔEvdw	ΔEele	ΔEpol	ΔEnonpol	ΔEMMPBSA	-TΔS	ΔGbind
AKT1-benzoylnapelline	-120.256±2.523	10.278±1.805	75.598±4.566	-16.246±0.093	-50.627±5.069	26.444±3.249	-24.183±8.219
EGFR-quercetin	-92.385±13.213	-92.385±13.213	-92.385±13.213	-92.385±13.213	-92.385±13.213	-92.385±13.213	-92.385±13.213
PIK3CA-DFV	-161.782±2.07	-161.782±2.07	-161.782±2.07	-161.782±2.07	-161.782±2.07	-161.782±2.07	-161.782±2.07
PIK3CB-DFV	-102.207±5.05	-102.207±5.05	-102.207±5.05	-102.207±5.05	-102.207±5.05	-102.207±5.05	-102.207±5.05
PIK3R1-sexangularetin	-120.439±3.698	-120.439±3.698	-120.439±3.698	-120.439±3.698	-120.439±3.698	-120.439±3.698	-120.439±3.698
SRC-deltoin	-115.35±3.196	-115.35±3.196	-115.35±3.196	-115.35±3.196	-115.35±3.196	-115.35±3.196	-115.35±3.196

Table 4. Pharmacokinetic properties of key active ingredients

Molecule	benzoylnapelline	Deltoin	DFV	Quercetin	Sexangularetin
GI absorption	High	High	High	High	High
BBB permeant	Yes	Yes	Yes	No	No
Pgp substrate	Yes	No	Yes	No	No
CYP1A2 inhibitor	No	Yes	Yes	Yes	Yes
CYP2C19 inhibitor	Yes	Yes	No	No	No
CYP2C9 inhibitor	No	Yes	No	No	No
CYP2D6 inhibitor	Yes	No	No	Yes	Yes
CYP3A4 inhibitor	No	Yes	No	Yes	Yes
log Kp (cm/s)	-6.68	-5.68	-6.23	-7.05	-6.46

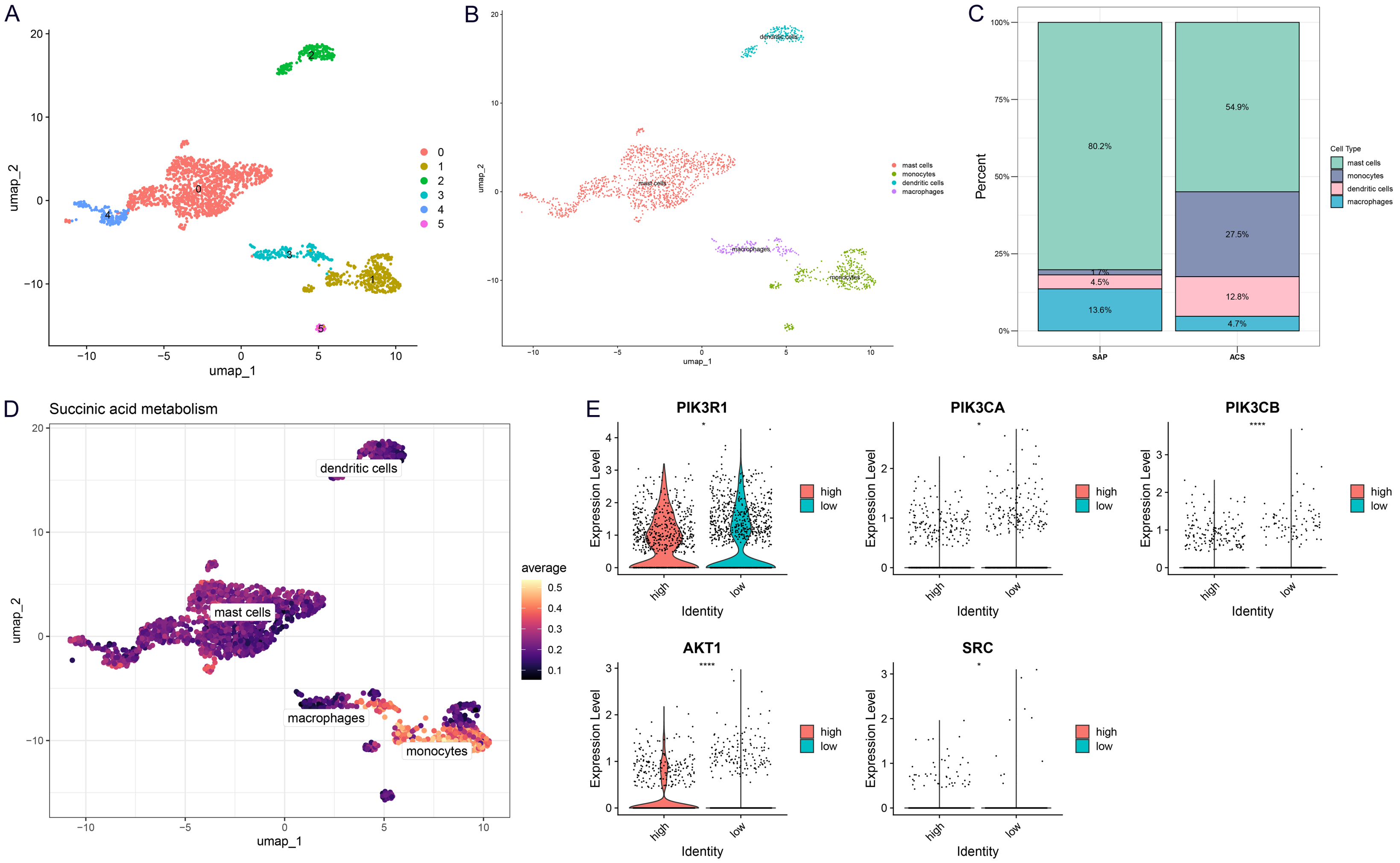

Figure 1. Identification of critical cell types. A. UMAP clustering plot of six clusters in the GSE171213 dataset. B. UMAP plot illustrating the distribution of four cell types. C. Cellular composition of each cell type in the samples. D. Mean score derived from five distinct algorithms evaluating the activity of intersection genes for each cell type. E. Inter-group differences in key target expression in monocyte high/low-score groups. **P* < 0.05, *****P* < 0.0001.

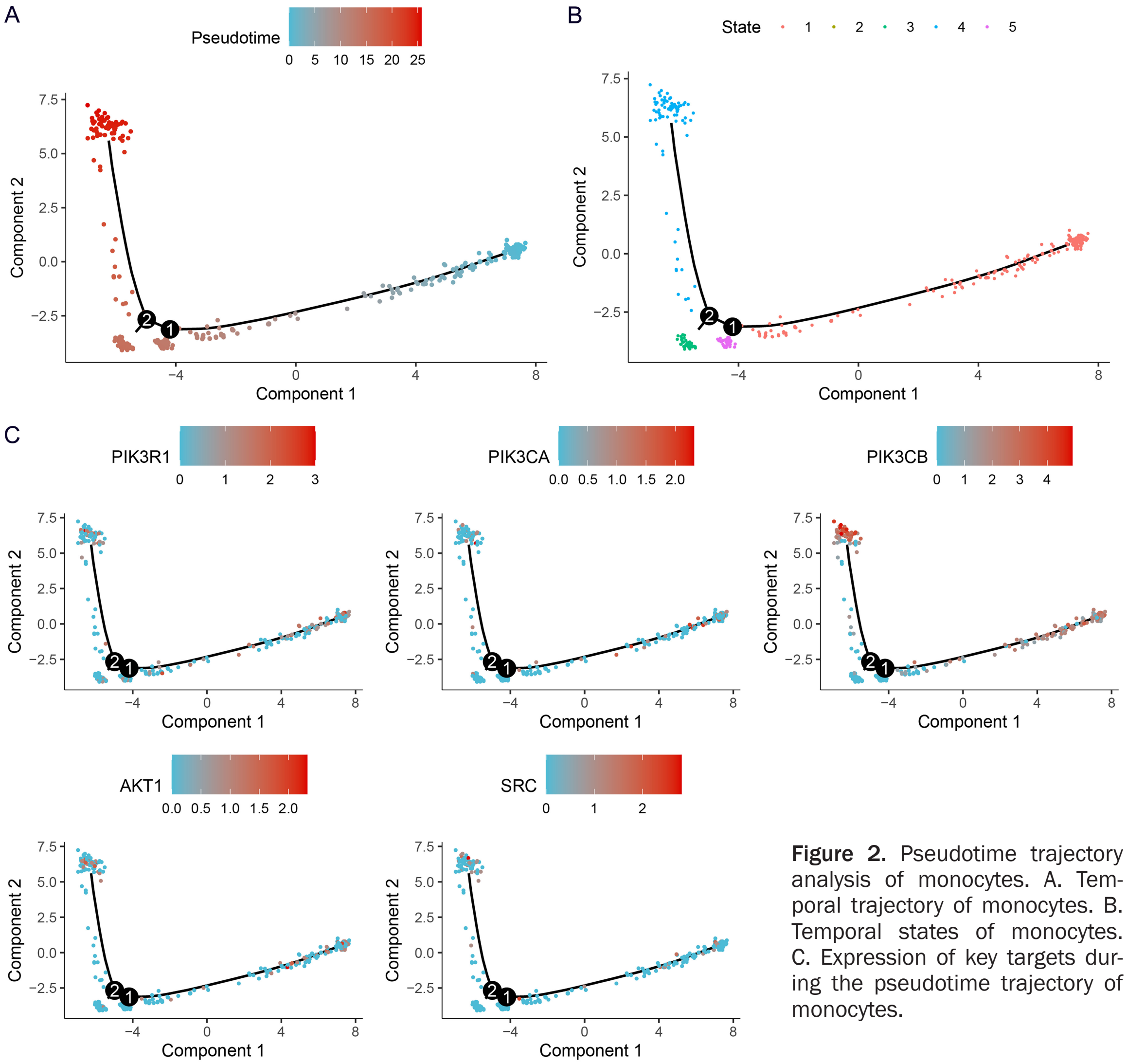

Figure 2. Pseudotime trajectory analysis of monocytes. A. Temporal trajectory of monocytes. B. Temporal states of monocytes. C. Expression of key targets during the pseudotime trajectory of monocytes.

which are mechanistically linked to BYXSF's therapeutic effects in post-PCI angina (**Figure 1D**). Significant differential expression of the six key targets in monocyte high/low-score groups further supports the drug → gene → cell → disease mechanistic axis (**Figure 1E**). Pseudotime trajectory analysis identified five distinct monocyte differentiation stages (**Figure 2A**, **2B**). Among key targets, PIK3CB was upregulated in both initial and terminal stages, while the others were stably expressed throughout differentiation (**Figure 2C**).

BYXSF alleviated post-PCI angina by modulating the PI3K-Akt and NF-κB pathways

To investigate BYXSF's mechanism of action, an I/R rat model was established and randomly divided into six groups: sham-operated (S) group, I/R model group, three BYXSF dose groups (low, medium, and high doses), and atorvastatin-treated group. Cardiac function was assessed using echocardiography (**Figure 3A**). Compared to the S group, the I/R model group had significantly reduced left ventricular EF% and FS%, while both high-dose BYXSF and atorvastatin treatments markedly improved EF% and FS% (**Figure 3B**, **3C**). H&E staining revealed that sham-operated rats had intact cardiac layers, uniform cardiomyocytes, and no inflammation, while model rats showed left ventricular necrosis, eosinophilic debris, connective tissue hyperplasia, marked lymphocytic infiltration, and neovascularization. All BYXSF treatment groups demonstrated dose-dependent improvements: low and medium doses reduced edema and improved fiber alignment,

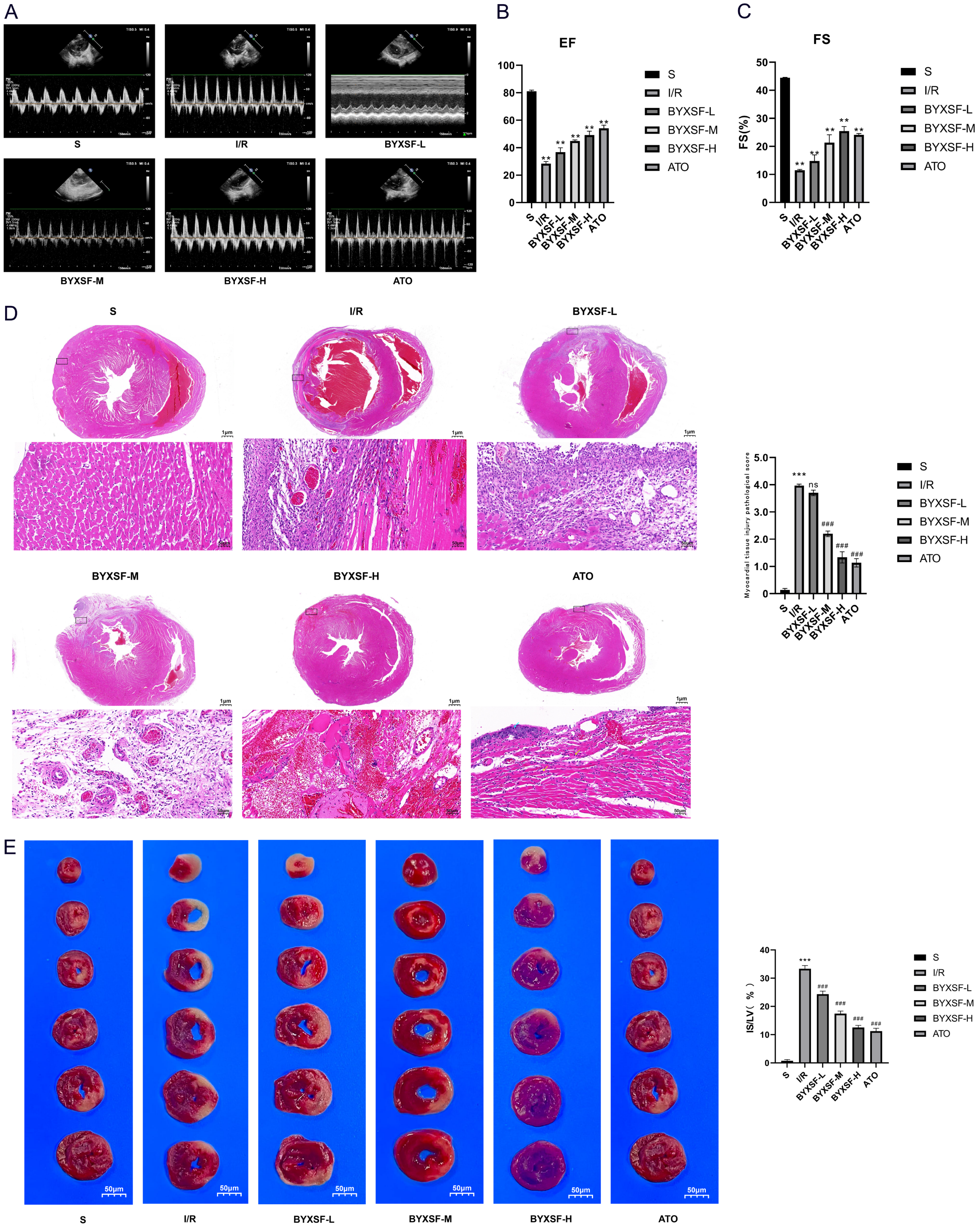

Figure 3. Construction and validation of I/R and treatment models for post-PCI angina. A. Echocardiographic images of rats in each group. B. Left ventricular ejection fraction (EF%) (n = 6). $^{**}P < 0.01$. C. Left ventricular fractional shortening (FS%) (n = 6). $^{**}P < 0.01$. D. Hematoxylin and eosin (H&E) staining results for animal models (×20). Compared to the S group, $^{***}P < 0.001$; compared to the I/R model group, $^{\#\#\#}P < 0.001$. ns indicates no significance. E. 2,3,5-triphenyltetrazolium chloride (TTC) staining results for animal models (×20). Compared to the S group, $^{***}P < 0.001$; compared to the I/R model group, $^{\#\#\#}P < 0.001$.

while the high-dose group showed restored membrane integrity, reduced inflammation, and improved fiber organization, comparable to atorvastatin's efficacy in restoring cellular morphology (**Figure 3D**). TTC staining confirmed intact hearts in the sham-operated group, while model hearts exhibited extensive myocardial infarction. BYXSF treatment dose-dependently reduced infarct size, with the high-dose group exhibiting the most significant protective effect. This was consistent with the histopathologic improvements in myocardial fiber arrangement and inflammation resolution (**Figure 3E**).

Given that I/R-induced cardiac injury involves both tissue necrosis and programmed cell death, TUNEL staining was employed to assess myocardial cell apoptosis. The results showed no positive cells detected in the S group, while the model group had a significantly increased rate of positive cells. In contrast, all BYXSF treatment groups displayed a marked reduction in apoptosis with a dose-dependent effect, and the anti-apoptotic protective effects were most prominent in the high-dose BYXSF group and the atorvastatin group (**Figure 4A**, **4B**). Serological tests revealed the I/R group had significantly elevated levels of IL-1β and TNF-α, increased cTnI content, and enhanced CK-MB release ($P < 0.01$), confirming the activation of the inflammation-oxidative stress-myocardial injury cascade. The high-dose BYXSF group effectively reversed these abnormal indicators ($P < 0.01$), and its efficacy was not statistically different from that of the atorvastatin group, revealing the molecular mechanism underlying its cardioprotective effect (**Figure 4C**). Further detection of the expression of proteins related to the PI3K-Akt and NF-κB signaling pathways (total AKT, phosphorylated AKT, NF-κB p65, phosphorylated NF-κB p65, total PI3K, and phosphorylated PI3K) showed that the expression of these proteins was significantly downregulated in the I/R group, while the BYXSF treatment groups exhibited a dose-dependent recovery. Notably, the protein expression profile of the high-dose BYXSF group was highly similar to that of the atorvastatin group (**Figure 4D**). RT-qPCR analysis indicated that compared to the S group, the mRNA expression levels of AKT, PI3K, and NF-κB in the model group were significantly decreased ($P < 0.01$). After 4 weeks of treatment, the mRNA levels of these molecules in all treatment groups were significantly increased compared to the model group ($P < 0.01$), among which the high-dose BYXSF group and atorvastatin group showed the most prominent upregulation effects (**Figure 4E**). In conclusion, these results confirmed that BYXSF exerts a therapeutic effect on post-PCI angina pectoris by regulating the PI3K-Akt and NF-κB signaling pathways.

Discussion

Percutaneous transluminal coronary angioplasty (PTCA) has significantly advanced, transforming from a high-risk invasive surgery into a common, very successful treatment. Nonetheless, the PCI invariably induces endothelial injury or loss [31], prompting local inflammatory cell infiltration [32] and leading to consequences such as post-PCI angina. Angina and coronary artery disease are important causes of heart-related readmission within 30 days and 1 year after PCI [33], among which up to 40% of patients experience persistent or recurrent angina pectoris within 3 years [34]. Abnormal myocardial metabolism is an important pathophysiologic factor leading to functional myocardial ischemia [21]. Compared to patients with myocardial infarction, the levels of TNF-α and C-reactive protein (CRP) in patients with unstable angina pectoris after PCI are significantly increased [35]. Data [36] have emphasized the importance of pro-inflammatory biomarkers in assessing the risk and prognosis of unstable angina pectoris. Given that coronary artery surgery may damage arteries and myocardium, leading to inflammation and white blood cell aggregation, addressing inflammation has become a promising therapeutic strategy.

This study established a regulatory network for BYXSF in the treatment of post-PCI angina, highlighting its multi-component, multi-target, and cascade-reaction attributes. Network analysis found 15 possible targets, with PIK3R1, PIK3CA, PIK3CB, EGFR, AKT1, and SRC were deemed as key nodes. Significant pathways including neuroactive ligand-receptor interaction, PI3K-Akt signaling, lipids and atherosclerosis, MAPK signaling, and calcium signaling were significantly enriched. The PI3K/Akt is essential for cardiovascular development: PIK3R1, PIK3CA, and PIK3CB function as regulatory and catalytic subunits, whereas Akt (protein kinase B) operates as a downstream effector [7]. Increased p-AKT expression indicates pathway activation, while p-AKT inhibition reduces the production of inflammatory cytokines [37, 38], indicating that pathway inhibi-

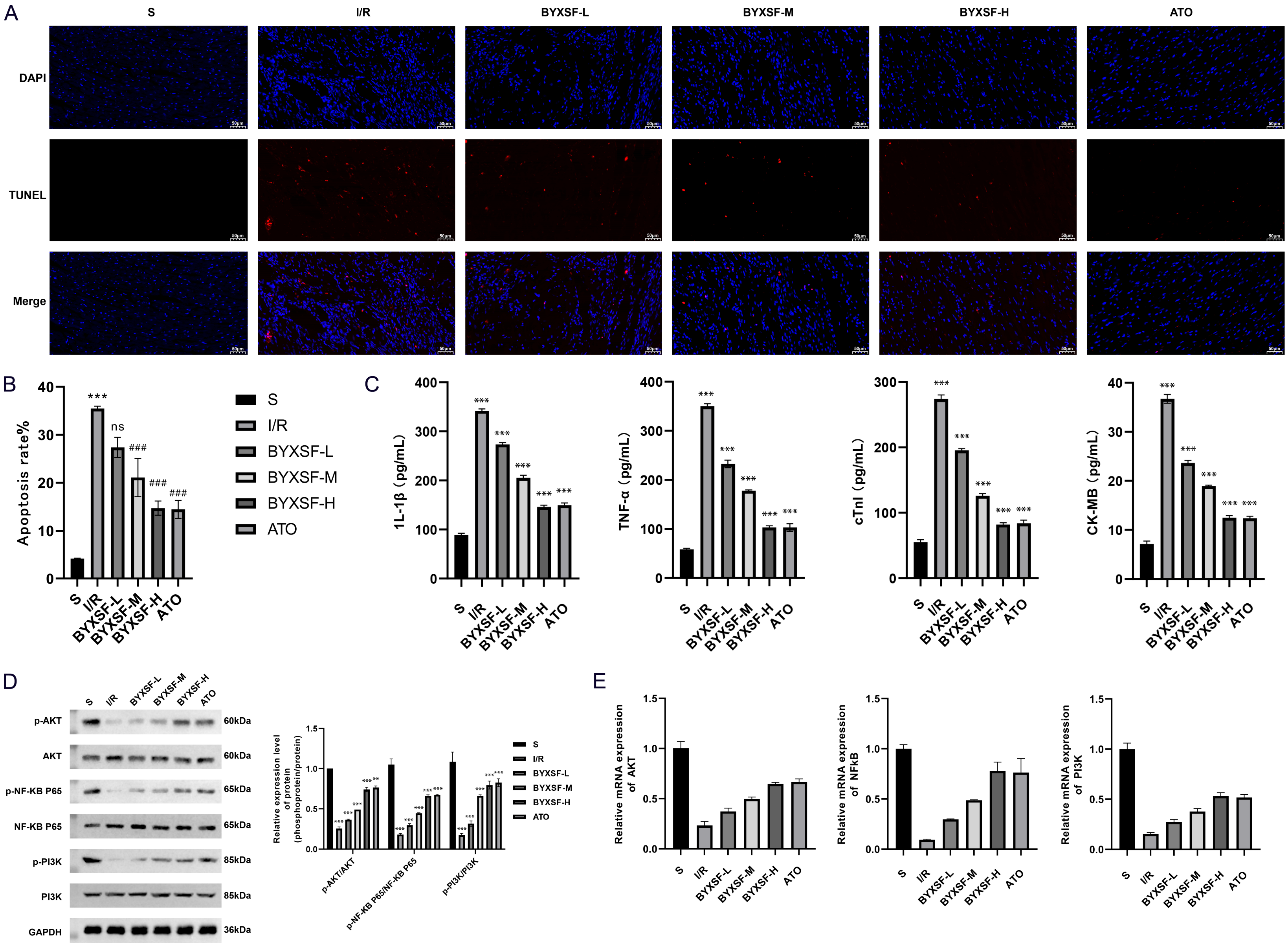
A
S
I/R
BYXSF-L
BYXSF-M
BYXSF-H
ATO
DAPI
TUNEL
Merge
50μm
B
Apoptosis rate%
40
30
20
10
0
***
ns
###
###
###
S
I/R
BYXSF-L
BYXSF-M
BYXSF-H
ATO
C
1L-1β（pg/mL）
TNF-α（pg/mL）
cTnI（pg/mL）
CK-MB（pg/mL）
400
300
200
100
0
***
D
p-AKT
AKT
p-NF-KB P65
NF-KB P65
p-PI3K
PI3K
GAPDH
60kDa
60kDa
65kDa
65kDa
85kDa
85kDa
36kDa
Relative expression level of protein (phosphoprotein/protein)
1.5
1.0
0.5
0.0
**
p-AKT/AKT
p-NF-KB P65/NF-KB P65
p-PI3K/PI3K
E
Relative mRNA expression of AKT
Relative mRNA expression of NFkB
Relative mRNA expression of PI3K

Figure 4. Expression of the phosphatidylinositol 3-kinase-AKT (PI3K-Akt) and Nuclear factor kappa-light-chain-enhancer of activated B cells (NF-κB) signaling pathway-related molecules at the protein and transcriptome levels. A. Myocardial cell apoptosis rates in each group (×20). Blue indicates normal cardiomyocytes, and red indicates apoptotic cells. B. Quantitative analysis of myocardial cell apoptosis rates. Compared to the S group, $^{***}P < 0.001$; compared to the I/R model group, $^{\#\#\#}P < 0.001$. ns indicates no significance. C. Serological tests of IL-1β, TNF-α, cTnI, and CK-MB for animal models. $^{***}P < 0.001$. D. Expression of PI3K-Akt and NF-κB signaling pathway-related proteins in animal models tested by western blotting. $^{**}P < 0.01$, $^{***}P < 0.001$. E. Expression of AKT, PI3K, and NF-κB at the transcriptome level. $^{**}P < 0.01$ compared to the S group.

tion may reduce inflammation. Activated Akt phosphorylates NF-κB, a transcription factor family regulating cardiac aging and cellular senescence [39], and targeting NF-κB can treat inflammation-related myocardial diseases [40]. PCI vascular injury activates the NF-κB pathway [41], in which SRC (non-receptor tyrosine kinase) acts as an upstream regulator, and EGFR (receptor tyrosine kinase) activates downstream pathways, including PI3K/Akt and NF-κB. BYXSF was found to simultaneously regulate apoptosis, inflammation, angiogenesis, and hypoxia responses.

Molecular docking revealed critical active compounds with appropriate target binding energy: benzoylnapelline, deltoin, DFV, quercetin, and sexangularetin. Benzoylnapelline, an aconitine alkaloid, may enhance myocardial energy metabolism remodeling and cardiomyocyte pluripotency [42]. DFV protects against myocardial ischemia through antioxidant and anti-apoptotic effects, alleviating mitochondrial dysfunction and inhibiting L-type calcium channels to decrease intracellular Ca^{2+} overload [43]. Deltoin binds stably to transforming growth factor β1 (TGFB1) and demonstrates anti-inflammatory properties [44]. Quercetin, a natural polyphenol, provides cardiovascular advantages through antioxidant and anti-inflammatory mechanisms [45]. Sexangularetin, a flavonoid compound, significantly reduces serum inflammatory factors [46]. These data substantiate the concept that BYXSF mitigates post-PCI angina chiefly by inhibiting inflammation.

The scRNA-seq analysis revealed four significant cell types: mast cells, monocytes, dendritic cells, and macrophages, of which monocytes and mast cells were the main populations. Monocytes play a key role in inflammation-driven neointimal hyperplasia and new atherosclerosis, as the initial cells in atherosclerosis [47], and promote myocardial fibrosis and dysfunction through pro-inflammatory changes in cardiac monocytes/macrophages [48]. They also play central roles in cardiac repair [49], possibly by regulating fibroblast activation in cardiac pathologies [50, 51]. During PCI, balloon dilation-induced plaque rupture stimulates macrophages and platelets to release tissue factor and vasoconstrictors, initiating coagulation and microthrombus formation that can block microcirculation and cause angina [52]. In a rat aortic injury model, BYXSF inhibited inflammation and significantly reduced serum IL-1β and TNF-α levels in myocardial I/R models.

The present research presents a new hypothesis: TNF-α, PI3K/AKT, and NF-κB constitute a cohesive regulatory network of inflammation, ischemia, and vascular processes that facilitates the pathogenic activation of monocytes, hence influencing the management of post-PCI angina. This discovery clarifies the molecular foundation of BYXSF and underscores its promise as a novel treatment alternative. However, there are limitations: 1) This study only focused on the PI3K-Akt and NF-κB pathways, without in-depth study of their cross-regulatory interactions or the specific mechanisms of the five active ingredients; 2) Due to the lack of *in vitro/ in vivo* safety assessment and the lack of determined clinical safe doses, the assessment of the toxicity of active ingredients needs to be further explored; 3) In view of the limited clinical trial data, the applicability analysis of subtypes is insufficient, which will hinder the clinical transformation of research results. Future studies will further verify the role of TNF-α-PI3K/AKT-NF-κB network in monocyte activation. We will elucidate the binding mechanism of target components and conduct multi-center large-scale trials to evaluate the efficacy, safety and optimal dose of BYXSF in different populations, aiming to establish it as a clinical treatment alternative.

Conclusion

This study illustrated that BYXSF provides cardioprotective effects through five principal active constituents (benzoylnapelline, quercetin, DFV, sexangularetin, and deltoin), which markedly reinstate the diminished phosphorylation levels of PI3K, AKT, and NF-κB in post-PCI angina. These findings elucidate the molecular basis for BYXSF's efficacy, identify essential bioactive constituents, and highlight the synergistic potential of natural compounds that target the PI3K/AKT and NF-κB pathways - presenting a novel multi-target approach for post-PCI angina. They endorse the logical use of TCM for cardiovascular protection, establish a chemical foundation for the quality control and pharmacologic enhancement of BYXSF, and may guide the formulation of novel combination therapies for post-PCI angina.

Disclosure of conflict of interest

None.

Address correspondence to: Xiaomin Jiao, The Second Affiliated Hospital of Liaoning University of Traditional Chinese Medicine, No. 60 Huanghe North Street, Huanggu District, Shenyang 110034, Liaoning, Shenyang, China. E-mail: 17718585947@163.com

References

[1] Ambrosio G, Collins P, Dechend R, Lopez-Sendon J, Manolis AJ and Camm AJ. Sta Ble Angina: Pe Rcept Ion of Nee Ds, quality of life and Mana Gem Ent of patients (BRIDGE Study)-a multinational European physician survey. Angiology 2019; 70: 397-406.

[2] Xing N, Long XT, Zhang HJ, Fu LD, Huang JY, Chaurembo AI, Chanda F, Xu YJ, Shu C, Lin KX, Yang K and Lin HB. Research progress on effects of traditional Chinese medicine on myocardial ischemia-reperfusion injury: a review. Front Pharmacol 2022; 13: 1055248.

[3] Ishii M, Kaikita K, Sato K, Yamanaga K, Miyazaki T, Akasaka T, Tabata N, Arima Y, Sueta D, Sakamoto K, Yamamoto E, Tsujita K, Yamamuro M, Kojima S, Soejima H, Hokimoto S, Matsui K and Ogawa H. Impact of statin therapy on clinical outcome in patients with coronary spasm. J Am Heart Assoc 2016; 5: e003426.

[4] Ferrari R, Pavasini R, Camici PG, Crea F, Danchin N, Pinto F, Manolis A, Marzilli M, Rosano GMC, Lopez-Sendon J and Fox K. Anti-anginal drugs-beliefs and evidence: systematic review covering 50 years of medical treatment. Eur Heart J 2019; 40: 190-194.

[5] Knuuti J, Wijns W, Saraste A, Capodanno D, Barbato E, Funck-Brentano C, Prescott E, Storey RF, Deaton C, Cuisset T, Agewall S, Dickstein K, Edvardsen T, Escaned J, Gersh BJ, Svitil P, Gilard M, Hasdai D, Hatala R, Mahfoud F, Masip J, Muneretto C, Valgimigli M, Achenbach S and Bax JJ; ESC Scientific Document Group. 2019 ESC Guidelines for the diagnosis and management of chronic coronary syndromes. Eur Heart J 2020; 41: 407-477.

[6] Long L, Lin S, Qin HZ, Xu LB, Zhang M and Lu ZL. Inhibitory effect of aqueous extract of Pteris multifida on lipopolysaccharide-induced inflammation in RAW264.7 cells. Chinese Journal of Traditional Chinese Medicinal Materials 2024; 47: 730-734.

[7] Adon T, Bhattacharya S, Madhunapantula SV and Kumar HY. Structural requirements of isoform-specific inhibitors of Akt: Implications in the development of effective cancer treatment strategies. Eur J Med Chem 2025; 287: 117334.

[8] Liu K, Sun SM, Liu ZY, Du YH, Xiao J, Shi QJ and Li X. Study on optimization of extraction process and antioxidant activity of volatile oil from Cinnamomum cassia. Journal of Liaoning University of Traditional Chinese Medicine 2025; 1-13.

[9] Han QR, Zhang YK and Liu MY. Research progress of antipyretic mechanism of traditional Chinese medicine. China Journal of Chinese Medicine 2013; 28: 1018-1020.

[10] Hassanien MA. Ameliorating effects of ginger on isoproterenol-induced acute myocardial infarction in rats and its impact on cardiac nitric oxide. J Microsc Ultrastruct 2020; 8: 96-103.

[11] Yan CL, An FY, Liu YQ, Su Y, Wang CX, Li JJ, Lyu XY and Deng J. Study on regulatory mechanism of Huangqi decoction on Bcl-2/NF-κB signal pathway in rats with brain injury induced by 12C6+ Ion radiation. Chinese Journal of Modern Applied Pharmacy 2021; 38: 1-7.

[12] Wei LW, Li JY, Yang J, Xia Y, Wang JY and Bai Y. Mechanism of astragaloside IV in inhibiting noise-induced blood pressure elevation in mice. Chinese Journal of Industrial Medicine 2025; 38: 438-441.

[13] Yang T, Li X, Lu Z, Han X and Zhao M. Effectiveness and safety of Xuefu Zhuyu decoction for treating coronary heart disease angina: a systematic review and meta-analysis. Medicine (Baltimore) 2019; 98: e14708.

[14] Zhou P, Lu S, Luo Y, Wang S, Yang K, Zhai Y, Sun G and Sun X. Attenuation of TNF-α-induced inflammatory injury in endothelial cells by Ginsenoside Rb1 via inhibiting NF-κB, JNK and p38 signaling pathways. Front Pharmacol 2017; 8: 464.

[15] Lu S, Luo Y, Zhou P, Yang K, Sun G and Sun X. Ginsenoside compound K protects human umbilical vein endothelial cells against oxidized low-density lipoprotein-induced injury via inhi-

bition of nuclear factor-κB, p38, and JNK MAPK pathways. J Ginseng Res 2019; 43: 95-104.

[16] Wu DM, Wang YJ, Han XR, Wen X, Li L, Xu L, Lu J and Zheng YL. Tanshinone IIA prevents left ventricular remodelling via the TLR4/MyD88/NF-κB signalling pathway in rats with myocardial infarction. J Cell Mol Med 2018; 22: 3058-3072.

[17] Xu HL, Wang TF and Zhang C. Research advances in pharmacological mechanism and application of Danshensu and its derivatives. Chinese Journal of Modern Applied Pharmacy 2021; 38: 237-243.

[18] Chen P, Gao Z, Guo M, Pan D, Zhang H, Du J and Shi D. Efficacy and safety of Panax notoginseng saponin injection in the treatment of acute myocardial infarction: a systematic review and meta-analysis of randomized controlled trials. Front Pharmacol 2024; 15: 1353662.

[19] Meng Y, Du Z, Li Y, Gao P, Song J, Lu Y, Tu P, Jiang Y and Guo X. The synergistic mechanism of total saponins and flavonoids in Notoginseng-Safflower pair against myocardial ischemia uncovered by an integrated metabolomics strategy. Biomed Pharmacother 2020; 130: 110574.

[20] Wang L, He Y, Zhang Y, Zhou H, Yu L, Yang J and Wan H. Effects of active components of Fuzi and Gancao compatibility on Bax, Bcl-2, and caspase-3 in chronic heart failure rats. Evid Based Complement Alternat Med 2016; 2016: 7686045.

[21] De Luca L, Rosano GMC and Spoletini I. Post-percutaneous coronary intervention angina: from physiopathological mechanisms to individualized treatment. Cardiol J 2022; 29: 850-857.

[22] Niccoli G, Montone RA, Lanza GA and Crea F. Angina after percutaneous coronary intervention: the need for precision medicine. Int J Cardiol 2017; 248: 14-19.

[23] Liu QY, Zhang DF, Wang BY, Zhao WB, Zhang TY, Sutcharitchan C and Li S. Network pharmacology: advancing the application of large language models in traditional Chinese medicine research. Science of Traditional Chinese Medicine 2025; 3: 113-123.

[24] Emoto T, Yamamoto H, Yamashita T, Takaya T, Sawada T, Takeda S, Taniguchi M, Sasaki N, Yoshida N, Saito Y, Sivasubramaniyam T, Otake H, Furuyashiki T, Robbins CS, Kawai H and Hirata KI. Single-Cell RNA sequencing reveals a distinct immune landscape of myeloid cells in coronary culprit plaques causing acute coronary syndrome. Circulation 2022; 145: 1434-1436.

[25] Shannon P, Markiel A, Ozier O, Baliga NS, Wang JT, Ramage D, Amin N, Schwikowski B and Ideker T. Cytoscape: a software environment for integrated models of biomolecular interaction networks. Genome Res 2003; 13: 2498-2504.

[26] Saikia S and Bordoloi M. Molecular docking: challenges, advances and its use in drug discovery perspective. Curr Drug Targets 2019; 20: 501-521.

[27] Sinelnikova A and Spoel DV. NMR refinement and peptide folding using the GROMACS software. J Biomol NMR 2021; 75: 143-149.

[28] Hao Y, Hao S, Andersen-Nissen E, Mauck WM 3rd, Zheng S, Butler A, Lee MJ, Wilk AJ, Darby C, Zager M, Hoffman P, Stoeckius M, Papalexi E, Mimitou EP, Jain J, Srivastava A, Stuart T, Fleming LM, Yeung B, Rogers AJ, McElrath JM, Blish CA, Gottardo R, Smibert P and Satija R. Integrated analysis of multimodal single-cell data. Cell 2021; 184: 3573-3587, e3529.

[29] McGinnis CS, Murrow LM and Gartner ZJ. DoubletFinder: doublet detection in single-cell RNA sequencing data using artificial nearest neighbors. Cell Syst 2019; 8: 329-337, e324.

[30] Trapnell C, Cacchiarelli D, Grimsby J, Pokharel P, Li S, Morse M, Lennon NJ, Livak KJ, Mikkelsen TS and Rinn JL. The dynamics and regulators of cell fate decisions are revealed by pseudotemporal ordering of single cells. Nat Biotechnol 2014; 32: 381-386.

[31] Bonello L, Harhouri K, Sabatier F, Camoin-Jau L, Arnaud L, Baumstarck-Barrau K, Ait-Mokhtar O, Roubille F, Piot C, Lesavre N, Paganelli F and Dignat-George F. Level of adenosine diphosphate receptor P2Y12 blockade during percutaneous coronary intervention predicts the extent of endothelial injury, assessed by circulating endothelial cell measurement. J Am Coll Cardiol 2010; 56: 1024-1031.

[32] Blum A, Schneider DJ, Sobel BE and Dauerman HL. Endothelial dysfunction and inflammation after percutaneous coronary intervention. Am J Cardiol 2004; 94: 1420-1423.

[33] Kwok CS, Shah B, Al-Suwaidi J, Fischman DL, Holmvang L, Alraies C, Bagur R, Nagaraja V, Rashid M, Mohamed M, Martin GP, Kontopantelis E, Kinnaird T and Mamas M. Timing and causes of unplanned readmissions after percutaneous coronary intervention: insights from the nationwide readmission database. JACC Cardiovasc Interv 2019; 12: 734-748.

[34] Crea F, Bairey Merz CN, Beltrame JF, Berry C, Camici PG, Kaski JC, Ong P, Pepine CJ, Sechtem U and Shimokawa H. Mechanisms and diagnostic evaluation of persistent or recurrent angina following percutaneous coronary revascularization. Eur Heart J 2019; 40: 2455-2462.

[35] Su Q, Li L, Zhao J, Sun Y and Yang H. Effects of trimetazidine on periprocedural microRNA-21 expression by CD4+ T lymphocytes in patients

with unstable angina pectoris. Oncotarget 2017; 8: 104992-104999.

[36] Zhang Z, Wang H, Wang R, She Z, Liang X, Liu H, Kou X and Wang S. Impact of white blood cell count after percutaneous coronary intervention on long-term prognosis in patients with unstable angina pectoris: a single-center retrospective observational cohort study. Vasc Health Risk Manag 2025; 21: 25-37.

[37] Zhang Z, Yang L, Wang B, Zhang L, Zhang Q, Li D, Zhang S, Gao H and Wang X. Protective role of liriodendrin in mice with dextran sulphate sodium-induced ulcerative colitis. Int Immunopharmacol 2017; 52: 203-210.

[38] Sahu BD, Kumar JM and Sistla R. Fisetin, a dietary flavonoid, ameliorates experimental colitis in mice: relevance of NF-κB signaling. J Nutr Biochem 2016; 28: 171-182.

[39] Morgado LAL, Rodrigues LMZ, Silva DCF, da Silva BD, Irigoyen MCC and Takano APC. NF-κB-specific suppression in cardiomyocytes unveils aging-associated responses in cardiac tissue. Biomedicines 2025; 13: 224.

[40] Hassen MD, Mousa NO, Radwan SM and Gabre RM. "The ameliorative effect of interleukin-17A neutralization on doxorubicin-induced cardiotoxicity by modulating the NF-κB/NLRP3/Caspase-1/IL-1β signaling pathway in rats". Inflammation 2025; 48: 2244-2257.

[41] Zou G, Zhu J, Liu Z, Wu L, Xu R, Chen H, Deng P and Deng C. Detoxification and activating blood circulation decoction reduces restenosis involving the TLR4/NF-κB pathway after balloon injury. Prostaglandins Other Lipid Mediat 2019; 140: 1-8.

[42] Liu H, Yue LX, Qiu LZ, Xiao CR, Wang SM, Zhou W and Gao Y. Continuous administration of low-dose aconitine remodels the mitochondrial energy metabolism pattern in hiPSCs-CM. Chinese Pharmacological Bulletin 2021; 37: 617-623.

[43] Zhang M, Qi J, He Q, Ma D, Li J, Chu X, Zuo S, Zhang Y, Li L and Chu L. Liquiritigenin protects against myocardial ischemic by inhibiting oxidative stress, apoptosis, and L-type Ca(2+) channels. Phytother Res 2022; 36: 3619-3631.

[44] Chang J, Jiang Z, Jin W, Wang Y, Li J, Chen J, Li H and Feng L. The molecular mechanism of traditional Chinese medicine prescription: Gutong formula in relieving osteolytic bone destruction. Biomed Res Int 2022; 2022: 4931368.

[45] Tang J, Diao P, Shu X, Li L and Xiong L. Quercetin and quercitrin attenuates the inflammatory response and oxidative stress in LPS-induced RAW264.7 cells: in vitro assessment and a theoretical model. Biomed Res Int 2019; 2019: 7039802.

[46] Huang XD, Zhong W, Qing B, Deng QM, Zhou GY and Wei JC. Intervention effect of Laggera alata extract on a mouse model of metabolism-associated fatty liver disease via upregulation of the Nrf2 signaling pathway. Drug Evaluation Research 2024; 47: 1971-1984.

[47] Hill MC, Kadow ZA, Long H, Morikawa Y, Martin TJ, Birks EJ, Campbell KS, Nerbonne J, Lavine K, Wadhwa L, Wang J, Turaga D, Adachi I and Martin JF. Integrated multi-omic characterization of congenital heart disease. Nature 2022; 608: 181-191.

[48] Simats A, Zhang S, Messerer D, Chong F, Beşkardeş S, Chivukula AS, Cao J, Besson-Girard S, Montellano FA, Morbach C, Carofiglio O, Ricci A, Roth S, Llovera G, Singh R, Chen Y, Filser S, Plesnila N, Braun C, Spitzer H, Gokce O, Dichgans M, Heuschmann PU, Hatakeyama K, Beltrán E, Clauss S, Bonev B, Schulz C and Liesz A. Innate immune memory after brain injury drives inflammatory cardiac dysfunction. Cell 2024; 187: 4637-4655, e4626.

[49] Rizzo G, Gropper J, Piollet M, Vafadarnejad E, Rizakou A, Bandi SR, Arampatzi P, Krammer T, DiFabion N, Dietrich O, Arias-Loza AP, Prinz M, Mack M, Schlepckow K, Haass C, Silvestre JS, Zernecke A, Saliba AE and Cochain C. Dynamics of monocyte-derived macrophage diversity in experimental myocardial infarction. Cardiovasc Res 2023; 119: 772-785.

[50] Hulsmans M, Sager HB, Roh JD, Valero-Muñoz M, Houstis NE, Iwamoto Y, Sun Y, Wilson RM, Wojtkiewicz G, Tricot B, Osborne MT, Hung J, Vinegoni C, Naxerova K, Sosnovik DE, Zile MR, Bradshaw AD, Liao R, Tawakol A, Weissleder R, Rosenzweig A, Swirski FK, Sam F and Nahrendorf M. Cardiac macrophages promote diastolic dysfunction. J Exp Med 2018; 215: 423-440.

[51] Amrute JM, Luo X, Penna V, Yang S, Yamawaki T, Hayat S, Bredemeyer A, Jung IH, Kadyrov FF, Heo GS, Venkatesan R, Shi SY, Parvathaneni A, Koenig AL, Kuppe C, Baker C, Luehmann H, Jones C, Kopecky B, Zeng X, Bleckwehl T, Ma P, Lee P, Terada Y, Fu A, Furtado M, Kreisel D, Kovacs A, Stitziel NO, Jackson S, Li CM, Liu Y, Rosenthal NA, Kramann R, Ason B and Lavine KJ. Targeting immune-fibroblast cell communication in heart failure. Nature 2024; 635: 423-433.

[52] Mangiacapra F, Bressi E, Di Gioia G, Pellicano M, Di Serafino L, Peace AJ, Bartunek J, Morisco C, Wijns W, De Bruyne B and Barbato E. Coronary microcirculation and peri-procedural myocardial injury during elective percutaneous coronary intervention. Int J Cardiol 2020; 306: 42-46.

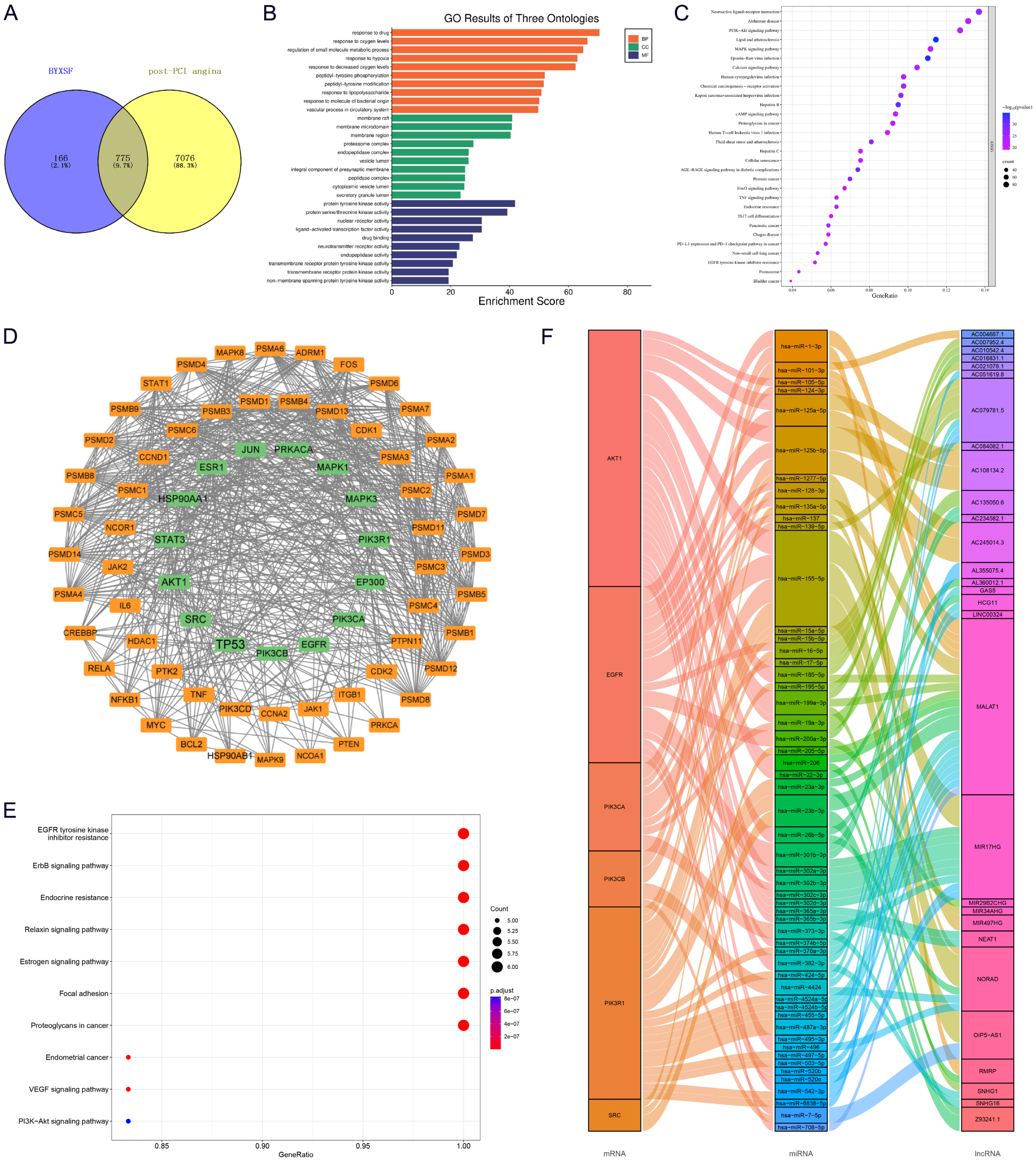

Figure S1. Identification of key targets. A. Venn diagram of 7,851 post-PCI angina target genes and 941 drug target genes. B. Top 10 Gene Ontology (GO) terms enriched by 775 intersection genes. C. Top 20 Kyoto Encyclopedia of Genes and Genomes (KEGG) pathways enriched by 755 intersection genes. D. Protein-protein interaction (PPI) network of targets with degree centrality > 17. E. KEGG pathways enriched by key targets. F. Long non-coding RNA (lncRNA)-microRNA (miRNA)-mRNA network of key targets.

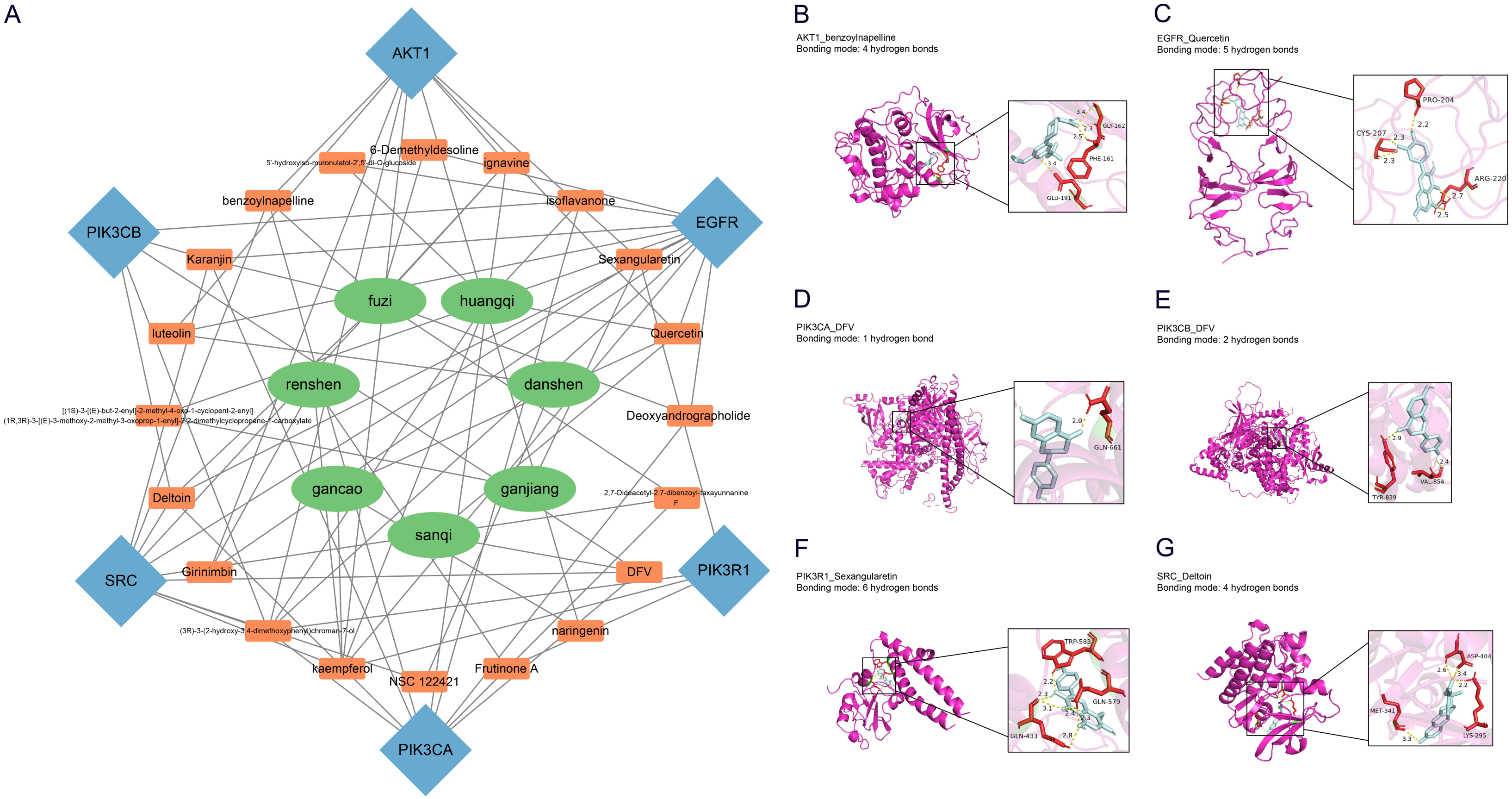

Figure S2. Herb-active component-key target-disease network and molecular docking of key targets. A. Herb-active component-key gene-disease network. B. Molecular docking between AKT1 and benzoylnapelline. C. Molecular docking between EGFR and quercetin. D. Molecular docking between PIK3CA and DFV. E. Molecular docking between PIK3CB and liquiritigenin (DFV). F. Molecular docking between PIK3R1 and sexangularetin. G. Molecular docking between SRC and deltoin.

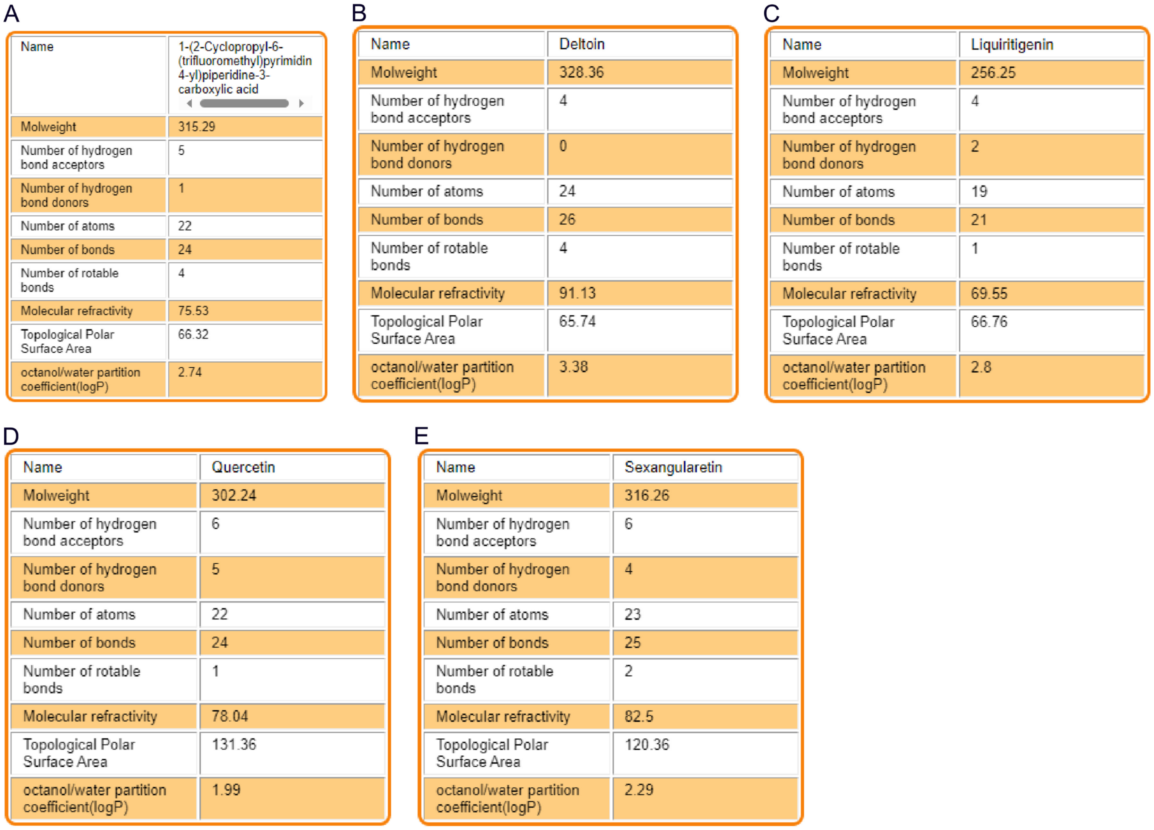

A

Name	1-(2-Cyclopropyl-6-(trifluoromethyl)pyrimidin 4-yl)piperidine-3-carboxylic acid
Molweight	315.29
Number of hydrogen bond acceptors	5
Number of hydrogen bond donors	1
Number of atoms	22
Number of bonds	24
Number of rotable bonds	4
Molecular refractivity	75.53
Topological Polar Surface Area	66.32
octanol/water partition coefficient(logP)	2.74

B

Name	Deltoin
Molweight	328.36
Number of hydrogen bond acceptors	4
Number of hydrogen bond donors	0
Number of atoms	24
Number of bonds	26
Number of rotable bonds	4
Molecular refractivity	91.13
Topological Polar Surface Area	65.74
octanol/water partition coefficient(logP)	3.38

C

Name	Liquiritigenin
Molweight	256.25
Number of hydrogen bond acceptors	4
Number of hydrogen bond donors	2
Number of atoms	19
Number of bonds	21
Number of rotable bonds	1
Molecular refractivity	69.55
Topological Polar Surface Area	66.76
octanol/water partition coefficient(logP)	2.8

D

Name	Quercetin
Molweight	302.24
Number of hydrogen bond acceptors	6
Number of hydrogen bond donors	5
Number of atoms	22
Number of bonds	24
Number of rotable bonds	1
Molecular refractivity	78.04
Topological Polar Surface Area	131.36
octanol/water partition coefficient(logP)	1.99

E

Name	Sexangularetin
Molweight	316.26
Number of hydrogen bond acceptors	6
Number of hydrogen bond donors	4
Number of atoms	23
Number of bonds	25
Number of rotable bonds	2
Molecular refractivity	82.5
Topological Polar Surface Area	120.36
octanol/water partition coefficient(logP)	2.29

Figure S3. Pharmacologic properties of key active ingredients. A. Pharmacologic properties of benzoylnapelline. B. Pharmacologic properties of deltoin. C. Pharmacologic properties of liquiritigenin (DFV). D. Pharmacologic properties of quercetin. E. Pharmacologic properties of sexangularetin.

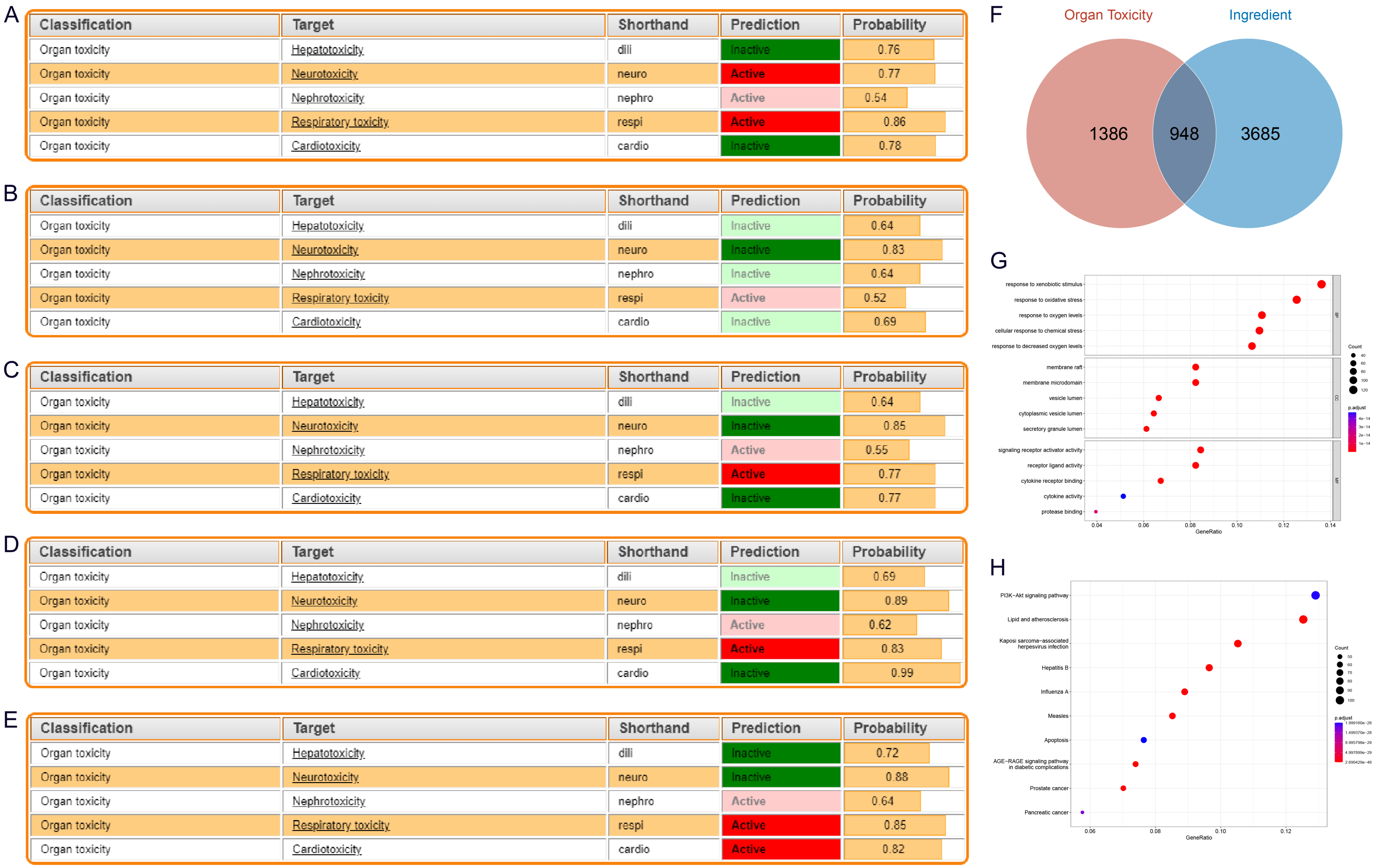

A

Classification	Target	Shorthand	Prediction	Probability
Organ toxicity	Hepatotoxicity	dili	Inactive	0.76
Organ toxicity	Neurotoxicity	neuro	Active	0.77
Organ toxicity	Nephrotoxicity	nephro	Active	0.54
Organ toxicity	Respiratory toxicity	respi	Active	0.86
Organ toxicity	Cardiotoxicity	cardio	Inactive	0.78

B

Classification	Target	Shorthand	Prediction	Probability
Organ toxicity	Hepatotoxicity	dili	Inactive	0.64
Organ toxicity	Neurotoxicity	neuro	Inactive	0.83
Organ toxicity	Nephrotoxicity	nephro	Inactive	0.64
Organ toxicity	Respiratory toxicity	respi	Active	0.52
Organ toxicity	Cardiotoxicity	cardio	Inactive	0.69

C

Classification	Target	Shorthand	Prediction	Probability
Organ toxicity	Hepatotoxicity	dili	Inactive	0.64
Organ toxicity	Neurotoxicity	neuro	Inactive	0.85
Organ toxicity	Nephrotoxicity	nephro	Active	0.55
Organ toxicity	Respiratory toxicity	respi	Active	0.77
Organ toxicity	Cardiotoxicity	cardio	Inactive	0.77

D

Classification	Target	Shorthand	Prediction	Probability
Organ toxicity	Hepatotoxicity	dili	Inactive	0.69
Organ toxicity	Neurotoxicity	neuro	Inactive	0.89
Organ toxicity	Nephrotoxicity	nephro	Active	0.62
Organ toxicity	Respiratory toxicity	respi	Active	0.83
Organ toxicity	Cardiotoxicity	cardio	Inactive	0.99

E

Classification	Target	Shorthand	Prediction	Probability
Organ toxicity	Hepatotoxicity	dili	Inactive	0.72
Organ toxicity	Neurotoxicity	neuro	Inactive	0.88
Organ toxicity	Nephrotoxicity	nephro	Active	0.64
Organ toxicity	Respiratory toxicity	respi	Active	0.85
Organ toxicity	Cardiotoxicity	cardio	Active	0.82

Figure S4. Prediction and enrichment analysis of toxic targets. A. Toxicity evaluation of benzoylnapelline. B. Toxicity evaluation of deltoin. C. Toxicity evaluation of liquiritigenin (DFV). D. Toxicity evaluation of quercetin. E. Toxicity evaluation of sexangularetin. F. Venn diagram of 2,334 visceral toxicity targets and 4,633 key active ingredient-related toxicity targets. G. GO terms enriched by toxicity targets. H. KEGG pathways enriched by toxicity targets.

Bu-Yi-Xin-Shen formula targetsmonocytes through PI3K-Akt/NF-κB pathway

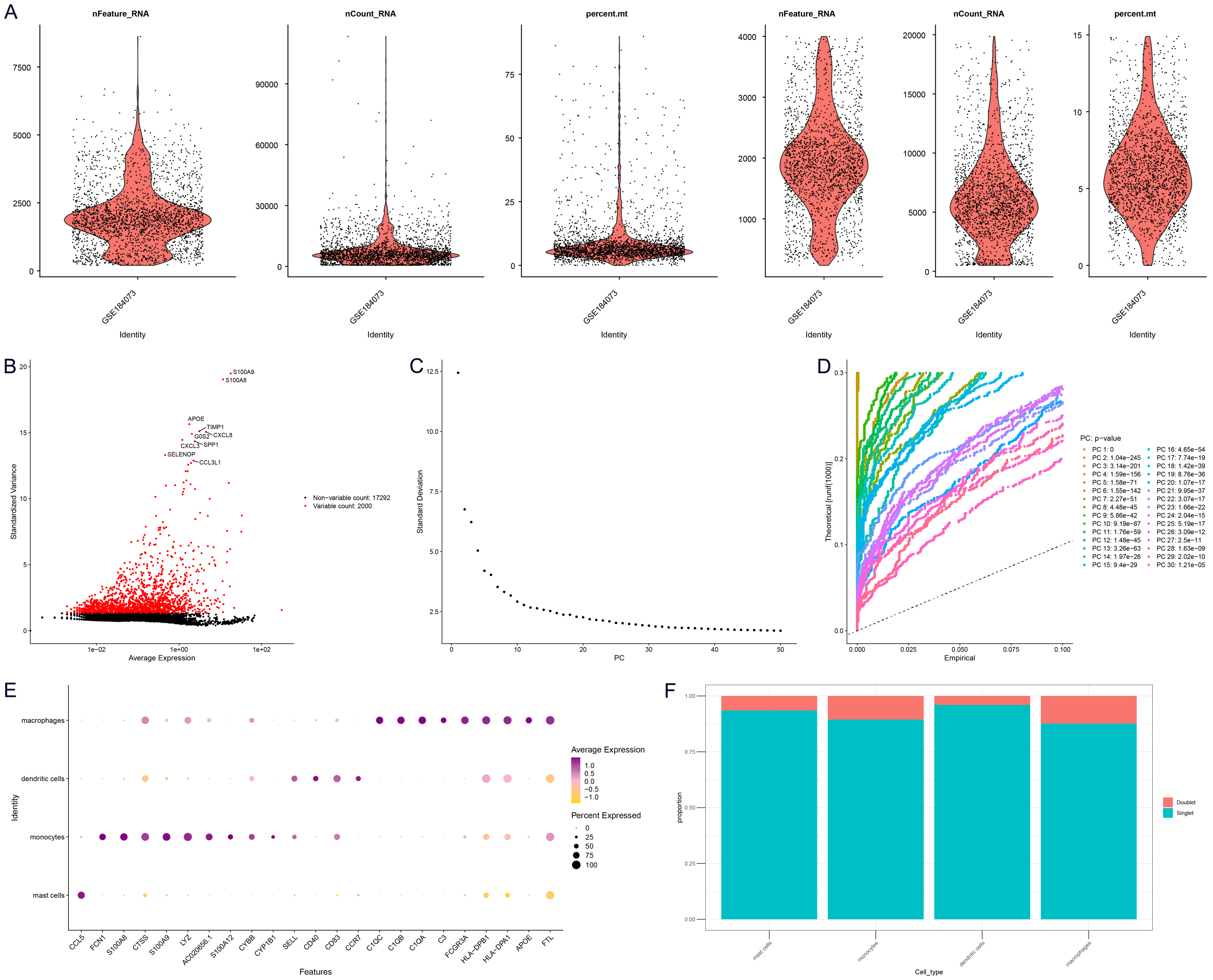

Figure S5. scRNA-seq data processing. A. scRNA-seq data before (left) and after (right) quality control. B. Selection of top 2,000 HVGs. C. Elbow plot of PCs. D. Permutation test for PCA. E. Expression of marker genes in cell types. F. The proportion of doublets in each cell type.